

Coordinated ground-based and space-based observations of equatorial plasma bubbles

Ercha Aa^{1,2}, Shasha Zou¹, Richard Eastes³, Deepak K. Karan³, Shun-Rong Zhang², Philip J. Erickson², and Anthea J. Coster²

¹Department of Climate and Space Sciences and Engineering, University of Michigan, Ann Arbor, MI, USA.

²Haystack Observatory, Massachusetts Institute of Technology, 99 Millstone Road, Westford, MA, USA.

³Laboratory for Atmospheric and Space Physics, University of Colorado, Boulder, CO, USA.

Key Points:

- Combined GOLD/UV spectrograph images and ground-based TEC data revealed EPB features and development over a large geographic area
- Bottomside F-layer oscillations and travelling ionospheric disturbance were observed by ionosonde and detrended TEC results
- Atmospheric gravity waves likely play an important role in seeding the R-T instability and the development of this EPB event

This is the author manuscript accepted for publication and has undergone full peer review but has not been through the copyediting, typesetting, pagination and proofreading process, which may lead to differences between this version and the [Version of Record](#). Please cite this article as doi: [10.1029/2019JA027569](https://doi.org/10.1029/2019JA027569)

Corresponding author: E. Aa, aercha@mit.edu

Abstract

This paper presents coordinated and fortuitous ground-based and space-borne observations of equatorial plasma bubbles (EPBs) over the South American area on 24 October 2018, combining the following measurements: Global-scale Observations of Limb and Disk (GOLD) far-ultraviolet emission images, Global Navigation Satellite System (GNSS) total electron content (TEC) data, Swarm in situ plasma density observations, ionosonde virtual height and drift data, and cloud brightness temperature data. The new observations from the GOLD/UV imaging spectrograph taken at geostationary orbit provide a unique opportunity to image the evolution of plasma bubbles near the F-peak height over a large geographic area from a fixed longitude location. The combined multi-instrument measurements provide a more integrated and comprehensive way to study the morphological structure, development, and seeding mechanism of EPBs. The main results of this study are as follows: (1) The bubbles developed a westward-tilted structure with 10° – 15° inclination relative to the local geomagnetic field lines, with eastward drift velocity of 80–120 m/s near the magnetic equator that gradually decreased with increasing altitude/latitude. (2) Wave-like oscillations in the bottomside F-layer and detrended TEC were observed, which are probably due to upward propagating atmospheric gravity waves (AGWs). The wavelength based on the MSTID signature was consistent with the inter-bubble distance of ~ 500 – 800 km. (3) The AGWs that originated from tropospheric convective zone are likely to play an important role in seeding the development of this equatorial EPBs event.

Plain Language Summary: This study presents multi-instrument observations of equatorial plasma density depletions occurred on 24 October 2018 by using Global-scale Observations of Limb and Disk (GOLD) far ultraviolet images, Global Navigation Satellite System (GNSS) total electron content (TEC) data, electron density measurements from Swarm satellite, ionosonde measurements, and cloud temperature data. This multi-instrument study generated an integrated and detailed image revealing both large-scale and meso-scale structures of the equatorial plasma depletion. Our results also suggest that atmospheric gravity waves originating from tropospheric convection activity could play a significant seeding role in the development of equatorial plasma bubbles.

1 Introduction

Equatorial plasma bubbles (EPBs) refer to irregular structures of plasma density depletion that are usually observed in the equatorial and low latitude F-region during postsunset period. Typical density irregularities within EPBs can have different scale sizes of several to hundreds of kilometers, and EPBs can cover a broad altitudinal range from the bottomside ionosphere up to $\sim 1,000$ km (Cherniak, Zakharenkova, & Sokolovsky, 2019; Lühr, Xiong, Park, & Rauberg, 2014). One of the top research priorities in the global space weather community is to better understand the generation mechanisms and the dynamic features of EPBs, because they can severely disrupt the amplitude and phase of trans-ionospheric radio waves so as to cause adverse effects on relevant communication and navigation systems. It is generally accepted that EPBs are triggered under a favorable condition of the generalized Rayleigh-Taylor (R-T) instability at the bottomside of the F layer, where a steep vertical density gradient forms after the E layer disappears post-sunset due to high recombination rate. During quiet times, the prereversal enhancement (PRE) of the zonal electric field is responsible for the enhanced upward $\mathbf{E} \times \mathbf{B}$ drift after sunset, which elevates the ionospheric height and subsequently amplifies the growth rate of R-T instability (Abdu, 2005; Carter, Zhang, Norman, Kumar, & Kumar, 2013; Fejer, Scherliess, & de Paula, 1999; Kil, 2015; Woodman & La Hoz, 1976). Thus, initial density perturbations at the bottomside F-layer can then evolve into EPBs and develop nonlinearly after rising to the topside ionosphere.

66 The morphological features and spatial/temporal variability of EPBs have been widely
67 investigated via case studies and statistical analysis using different observational meth-
68 ods. For example, the structure of EPBs can be observed from irregular traces of range-
69 type equatorial spread F (ESF) in ionograms (Abdu, 2012; Hysell, 2000; Li et al., 2018;
70 Tsunoda, 2015). The spatial variation of EPBs can be derived from the dark streaks of
71 emission depletion in optical observations from ground-based all-sky imagers (ASIs) or
72 space-based ultraviolet imaging spectrographs (e.g., Comberiate & Paxton, 2010; Hickey
73 et al., 2018; Kelley et al., 2003; Kil, Heelis, Paxton, & Oh, 2009; Makela, 2006; Marti-
74 nis et al., 2015; Otsuka, Shiokawa, Ogawa, & Wilkinson, 2002; Shiokawa, Otsuka, Lynn,
75 Wilkinson, & Tsugawa, 2015). In addition, the altitudinal information of irregularities
76 embedded within EPBs can be examined through observations of plume-like structures
77 from coherent backscatter radar or incoherent scatter radar measurements (Ajith et al.,
78 2015; Jin et al., 2018; Li et al., 2013; Rodrigues et al., 2018; Tulasi Ram, Ajith, Yokoyama,
79 Yamamoto, & Niranjana, 2017; Yokoyama & Fukao, 2006). Furthermore, the temporal
80 variation and occurrence distribution of irregularities/bubbles can be extracted from in
81 situ satellite observations, such as the Defense Meteorological Satellite Program (DMSP)
82 constellation (Burke, Gentile, Huang, Valladares, & Su, 2004; Burke, Huang, Gentile, &
83 Bauer, 2004; C. Y. Huang, Burke, Machuzak, Gentile, & Sultan, 2002), Communications/Navigation
84 Outage Forecasting System (C/NOFS) satellite (C.-S. Huang et al., 2014; Smith & Heelis,
85 2017), and Swarm constellation (Xiong et al., 2016; Zakharenkova, Astafyeva, & Cher-
86 niak, 2016). Moreover, with the fast-growing and global availability of ground-based Global
87 Navigation Satellite Systems (GNSS) measurements and space-based radio occultation
88 data, the evolution characteristics of EPBs can be monitored continuously on both global
89 or regional scales (e.g., Aa et al., 2018; Barros, Takahashi, Wrasse, & Figueiredo, 2018;
90 Buhari et al., 2014, 2017; Cherniak, Krankowski, & Zakharenkova, 2014; Cherniak & Za-
91 kharenkova, 2016; Katamzi-Joseph, Habarulema, & Hernández-Pajares, 2017; Ma & Maruyama,
92 2006; Nishioka, Saito, & Tsugawa, 2008; Takahashi et al., 2015).

93 Although EPBs have been extensively studied for several decades, there are still
94 some important and challenging tasks that need to be performed to improve current un-
95 derstanding of their detailed spatial/temporal structures and seeding mechanisms. In
96 this regard, different instruments have their own advantages and limitations in analyz-
97 ing EPBs: (1) Coherent/incoherent scatter radars can monitor irregularities at high spa-
98 tial resolution, but their location and field-of-view (FOV) limit their coverage range. (2)
99 Optical measurements of ASIs are limited with their field-of-view, and their availabil-
100 ity depends on weather conditions. For this reason, multiple ASIs are usually required
101 to get a complete evolution of EPBs structures. (3) Low-Earth orbiting (LEO) satellite
102 observations can produce in situ density profiles or ultraviolet radiance images of irreg-
103 ularities at high spatial resolution, but they can only sample a narrow swath of the EPBs
104 structures along the track of the satellite. (4) Global/regional GNSS total electron con-
105 tent (TEC) observations can monitor ionospheric variability continuously; however, the
106 small-scale structures characteristic of EPBs will sometimes be smoothed out because
107 of the integrating nature of the TEC calculation, not to mention huge data gaps which
108 still exist over receiver-sparse areas, such as oceans.

109 For these reasons, collective analysis of multi-site and multi-instrument measure-
110 ments provides an effective way to generate an integrated and comprehensive image for
111 specifying both large-scale and mesoscale features of plasma bubbles (e.g., Aa et al., 2019;
112 Cherniak et al., 2019). Recently, with the successful launch and deployment of NASA's
113 Global-scale Observations of Limb and Disk (GOLD) mission, an excellent opportunity
114 exists to use the unique data-set from the GOLD far ultraviolet (FUV) imaging spec-
115 trograph to monitor equatorial ionospheric structure. In this paper, we present coordi-
116 nated ground-based and space-borne observations of an EPBs event which occurred on
117 October 24, 2018. Our analysis uses multi-instrument measurements: GOLD/UV imag-
118 ing spectrograph, TEC from GNSS receiver networks, Swarm in-situ density observa-
119 tions, ionosonde measurements, and cloud temperature data. We use these observations

120 to implement a comprehensive analysis of the structural evolution and relevant seeding
121 mechanisms of EPBs.

122 2 Data Description

123 The GOLD mission was launched on 25 January 2018 and started its operational
124 observations in October 2018. The main scientific objective of GOLD is to understand
125 the “weather” response of the Earth’s thermosphere and ionosphere system to forcing
126 from above and below, and the formation and evolution of equatorial plasma bubbles
127 is a primary scientific question (Eastes et al., 2017, 2019). Operating at geostationary
128 orbit (GEO) over the longitude of 47.5°W, GOLD has an unparalleled advantage of “star-
129 ing” at the American region from a fixed geographic location for extended periods of time,
130 providing an exact time-evolving map that can unambiguously specify the spatiotem-
131 poral variability of Earth’s thermosphere and ionosphere system. The GOLD instrument
132 is a far-ultraviolet imaging spectrograph that measures Earth’s airglow emissions from
133 132 to 162 nm, which can be used to infer thermospheric temperature and composition
134 on the dayside disk as well as equatorial ionospheric structures on the nightside. The night-
135 time disk images of atomic oxygen 135.6 nm emissions, which have a spatial resolution
136 ~ 100 km in the longitudinal direction and ~ 50 km in the latitudinal direction, will be
137 used in this study to derive valuable information on the low latitude ionosphere.

138 Gridded TEC products from the Madrigal distributed data system are also used
139 to study EPBs structures. TEC data are produced and provided through the Madrigal
140 distributed data system developed at the Massachusetts Institute of Technology (MIT)’s
141 Haystack Observatory by using dense networks of worldwide GNSS receivers, and have
142 a resolution of 1° (latitude) $\times 1^\circ$ (longitude) $\times 5$ min (Rideout & Coster, 2006; Vier-
143 inen, Coster, Rideout, Erickson, & Norberg, 2016). Moreover, ionosonde measurements
144 from Sao Luis (2.6°S, 315.8°E) and Fortaleza (3.9°S, 321.6°E), as well as in situ plasma
145 density measurements onboard the Swarm A/C satellites are also used here to analyze
146 the characteristics of plasma irregularities.

147 Localized gravity waves that originated from the tropospheric convective zone could
148 be an essential factor in seeding EPBs, and the deep convection activity can be deduced
149 from cloud temperature data. These data are derived from global (60°S–60°N) 4-km pixel-
150 resolution infrared brightness temperature data, merged from selected geostationary satel-
151 lites measurements over the period of record (i.e., Geosynchronous Operational Environ-
152 mental Satellites [GOES]-8/9/10/11/12/13/14/15/16, United States; the Meteorolog-
153 ical Satellite [Meteosat]-5/7/8/9/10, European Community; Geosynchronous Meteorolo-
154 gical Satellite [GMS]-5/Multi-functional Transport Satellite [MTSat]-1R/2/Himawari-
155 8, Japan) (Janowiak, Joyce, & Xie, 2017).

156 3 Results

157 EPBs are known to produce optical signatures observed as streaks of reduced emis-
158 sion in space-borne ultraviolet imaging spectrographs (Kelley et al., 2003; Kil et al., 2004).
159 Figure 1 shows continuous OI 135.6 nm radiance maps observed by GOLD in successive
160 disk scans during 21:10–22:55 UT on 24 October 2018. The bright zonal band in the low-
161 latitude region paralleling the magnetic equator (red line) is produced by enhanced oxy-
162 gen ion density in the equatorial ionization anomaly (EIA) region. The dark streaks that
163 cut through the EIA band represent reduced emissions caused by low density within plasma
164 bubbles. There are seven discernible dark streaks marked with #1–7 from east to west.
165 These streaks elongate from northwest to southeast direction, with a meridional length
166 of $\sim 1,500$ – $2,000$ km and inter-bubble distance of ~ 500 – 800 km. Moreover, Figure 2 dis-
167 plays similar UV images for later time periods of 23:10–23:55 UT on October 24, 2018.
168 The white dotted curves show four different geomagnetic field lines (marked with I, II,
169 III, and IV) along which the EPBs were approximately extending. When comparing the

consecutive images, the EPBs depletion streaks were found to be drifting eastward and developing westward-tilted (or backward C-shape) structure. The tilt angle ranges from 10° – 15° relative to the Earth’s magnetic field line (Figure 2c and 2d). The airglow signature of EPBs and the tilted structure were also illustrated in simulations (e.g. Retterer, 2010) and are consistent with the previous ground-based and space-borne observations (Jin et al., 2018; Kelley et al., 2003; Kil et al., 2009; Li et al., 2018; Tsunoda, Livingston, McClure, & Hanson, 1982), which will be further discussed in the next section.

Besides the UV images, the EPBs can also be observed in two-dimensional TEC maps as a depletion structure perpendicular to the geomagnetic equator. Figure 3 shows twelve successive TEC maps over the South American region with 15-min cadence during 21:00–23:45 UT on 24 October 2018. The EIA crests can be seen as two regions with enhanced TEC about 10 degrees north and south of the geomagnetic equator (black dotted line). Two TEC depletion belts are parallel to the magnetic field lines, as highlighted by the black dashed lines, which exist over the equatorial region around 45° W and 40° W. Comparing with the surrounding region, the amplitude of the TEC depletion within these EPBs is approximately 10 TEC Unit (TECU, 10^{16} el/m²). Taking the left-side branch of the depletion as an example, we find an onset time of around 22 UT with a subsequent gradual extension toward the EIA crest along the geomagnetic field line “I”, which is the same field line as that marked in Figure 2. The EPB along field line “II” also exhibited similar but weaker evolution.

Moreover, there are two ionosondes, i.e., Sao Luis and Fortaleza, which are located near these two depletion belts and are labeled as asterisk and diamond in Figure 3. Figure 4 shows the F-layer bottomside virtual height (h’F), vertical drift velocity, and zonal drift velocity measured by these two ionosondes on 24 October 2018 (red), as compared with the previous 5-day averaged values (black). It can be seen from the top panels that the h’F over Sao Luis exhibited a significant pre-reversal enhancements (PREs, marked with an arrow) from 250 km to 360 km at around 21 UT on 24 October, while the 5-day averaged peak value of PREs is less than 300 km. A considerable h’F elevation around the same time can be also observed for Fortaleza station, with the peak value of PREs (310 km) on 24 October larger than 5-day average one (250 km). The corresponding peak velocity of vertical drift shown in Figures 4c and 4d, which is 30 m/s over Sao Luis and 25 m/s over Fortaleza, also displayed considerable increase compared with the 5-day averaged values (~ 10 m/s). These collectively demonstrate the presence of an enhanced dusk sector zonal electric field, raising the F layer and amplifying the growth rate of the R-T instability to generate the observed EPBs. The zonal drift exhibited eastward velocity after the PREs.

The nighttime GOLD/UV OI 135.6 nm images were mainly fixed at the American-Atlantic longitudes. The TEC maps have a broader coverage but with data gaps over the ocean, especially near the Northern Hemisphere part of the EIA. These two datasets complement each other and thus were combined to generate a map shown in Figure 5, which provides a much broader spatial context for EPBs. The extension of EPBs to the southern EIA crest and the backward C-shape streak spanning both hemispheres are clearly indicated. Furthermore, three consecutive satellite passes of Swarm A/C and the corresponding latitudinal profiles of the in situ electron density along these orbits are also shown in Figure 5. Both Swarm A and Swarm C flew at the height of ~ 450 km and were located at nearby longitudes around 09 LT (dayside) and 21 LT (nightside). Swarm B is not shown here since it did not pass through the American sector at local dusk hours during this period. The signature of plasma irregularities can be clearly seen in orbit #1 (17.0° W) of Swarm A during 22:00–22:30 UT and orbit #5 (39.0° W) of Swarm C during 23:30–00:00 UT, where considerable plasma density bite outs with sawtooth-like irregular fluctuations were measured near the magnetic equator (horizontal dotted line). This revealed the presence of small-scale density fluctuations within the EPBs seen in the GOLD/UV imaging and GNSS TEC results. Although Swarm A and C were very

close to each other and passed the EPBs nearly the same time, there are certain spatial differences in the small-scale structures that are observed by them (e.g., compare panels 1 and 4).

4 Discussion

First, the development of the westward tilt (or backward C-shape) of the EPBs depletion has been clearly shown in GOLD/UV optical images in Figure 1 and Figure 2. This shape has previously been suggested to be caused by latitudinal variation of zonal plasma drift and/or the polarization electric field inside the EPBs. As described in the principle of F-region dynamo theory (Rishbeth, 1997): the neutral wind in the post-sunset sector is typically eastward at low latitudes, which generates a downward F-region dynamo electric field. This vertical electric field further drives an eastward $\mathbf{E} \times \mathbf{B}$ drift of the F-region plasma with nearly similar velocities as the neutral wind. During this study event, estimation of the eastward drift velocity of 80–120 m/s near the magnetic equator can be achieved through comparing the differences ($\sim 2^\circ$ – 3°) of the central location of the dark streaks #1 between Figure 2a and 2d, which is consistent with the zonal drift velocities measured by ionosondes in Figures 4e and 4f and previous experimental/modeling studies of EPBs zonal drift velocities (e.g. Chapagain et al., 2012; Gurav et al., 2018; Huba, Ossakow, Joyce, Krall, & England, 2009; Sun et al., 2016). Furthermore, both numerical calculations and in situ observations have previously shown that this zonal plasma eastward drift often decreases with increasing altitude/latitude and thus forming a backward C-shape (e.g., Kil, Kintner, de Paula, & Kantor, 2002; Martinis, Eccles, Baumgardner, Manzano, & Mendillo, 2003; Pimenta, Fagundes, Sahai, Bittencourt, & Abalde, 2003). On the other hand, Kil et al. (2009) and C.-S. Huang et al. (2010) suggested that a polarization electric field can develop inside the plasma depletion region due to conductivity gradients, which can also retard the eastward flow of the plasma depletion structures.

Second, in addition to generally favorable condition for the R-T instability created by the usual Pre-reversal enhancement, various mechanisms have been proposed as possible seeding factors that can trigger initial plasma density perturbations on the bottom side F layer. These include: (1) Enhanced zonal eastward electric field due to solar wind-magnetosphere-ionosphere coupling processes. The prompt penetration electric field (PPEF) from high latitude to low latitude can increase the F-layer vertical drift on the daytime through dusk sectors and thus facilitate the development of EPBs (Abdu et al., 2003; Basu et al., 2007; Ebihara & Tanaka, 2015; Tulasi Ram et al., 2008). (2) Gravity waves (GWs) from the lower atmosphere. Gravity waves generated by upward propagating meteorological processes in the lower atmosphere may modulate the bottomside F-layer plasma, producing large-scale wave structures (LSWS) with periodic spacing, which may accelerate the F-layer uplifting and trigger EPBs (Abdu et al., 2009; McClure, Singh, Bamgboye, Johnson, & Kil, 1998; Retterer & Roddy, 2014; Tsunoda, 2010; Tsunoda et al., 2011; Tulasi Ram et al., 2014). (3) Neutral wind shear. Some studies suggested that vertical shear in the zonal winds could cause wave-like vortex, which has a rapid growth rate that can seed the R-T instability and initiate plasma irregularities (Hysell, Kudeki, & Chau, 2005; Hysell, Larsen, Swenson, & Wheeler, 2006; Kudeki, Akgiray, Milla, Chau, & Hysell, 2007). (4) Nighttime medium-scale travelling ionospheric disturbances (MSTIDs) due to Perkins/Es instabilities (Perkins, 1973). The polarization electric field within MSTIDs can map along the geomagnetic field lines to the equatorial bottomside F layer to initiate the EPBs (Krall et al., 2011; Miller, Makela, & Kelley, 2009; Taori et al., 2015; Valadares & Sheehan, 2016).

For the current EPBs case, the geomagnetic activity condition was relatively quiet on 24 October 2018 with the interplanetary magnetic field (IMF) B_z close to zero and no geomagnetic storm or substorm onset within a few hours before the observed EPBs (Figure 6a). The possibility of significant external driving forces (e.g., interplanetary electric fields) from the magnetosphere for EPBs in the postsunset sector is unlikely under

275 this circumstance. Figure 6b displays the rate of TEC index (ROTI) map to illustrate
276 the ionospheric irregularities between 35°W and 55°W over the South American sector.
277 Next, we discuss the possibility of forcing from below. Figure 6c shows the temporal vari-
278 ation of the electron density profile at Sao Luis between 12 and 24 UT on October 24,
279 2018. Of particular note, the ionosonde-retrieved topside profile above the F2 peak is
280 obtained assuming a α -Chapman shape of plasma distribution (Reinisch & Huang, 2001),
281 and thus only the bottomside profile should be examined. Three continuous quasi-periodic
282 (~ 50 min) wave-like modulations of the bottomside F-layer height marked by white ar-
283 rows can be clearly seen between 22–24 UT. Moreover, Figure 6d shows the F-layer true
284 height as observed by the digisonde at specific plasma frequencies (3.0–6.5 MHz) over
285 Sao Luis, plotted from 18 UT to 24 UT. There was a clear downward phase propaga-
286 tion (marked with a dashed line), which identifies the possible presence of atmospheric
287 gravity waves (Abdu et al., 2009; Mandal et al., 2019). Furthermore, Figure 6e shows
288 a keogram plot of detrended TEC as a function of latitude and time at 48°W longitude
289 that around the EPBs region. Detrended TEC was calculated using the same method
290 mentioned in Coster et al. (2017) and Zhang et al. (2017), where 1-hour TEC moving
291 average was subtracted. Medium-scale travelling ionospheric disturbances (MSTIDs) that
292 represent the ionospheric signature of atmospheric gravity waves are clearly observed in
293 detrended TEC. Several possible TID wavefronts (marked with dashed lines) can also
294 be clearly seen with an estimated propagation velocity of ~ 200 – 300 m/s and wavelength
295 of ~ 500 – 800 km. The latter is close to the value of inter-bubble distance shown in GOLD/UV
296 and TEC images. Many studies have demonstrated that such atmospheric gravity waves
297 can be generated in the tropospheric convective region near the inter-tropical convergence
298 zone (ITCZ) and can grow exponentially when propagating all the way upward into the
299 thermosphere-ionosphere system before being entirely dissipated (Li et al., 2016; Vadas,
300 2007; Yiğit et al., 2012; Yizengaw & Groves, 2018). However, considering that troposphere
301 excitation sources can be highly mobile and that wave propagation along the long path
302 is strongly influenced by low atmosphere variability, the manifestation of TIDs in the keogram
303 might not be so regular and well-organized. Thus, in order to further specify the poten-
304 tial source of the AGW/TIDs, Figure 6f shows an observation of deep clouds in bright-
305 ness temperature at 22 UT on 24 October 2018. The purple to blue areas in South Amer-
306 ican and West African areas indicates that temperature was lower than 210 K, a signa-
307 ture suggesting that the tops of thunderstorms protrude well into the tropopause region
308 (Hoffmann & Alexander, 2010). Such objects are referred to as deep convective clouds
309 and can be an important source for the generation of upward propagating AGWs (e.g.,
310 Azeem et al., 2015; Jonah et al., 2018; Vadas & Liu, 2009). In particular, these studies
311 indicated that concentric secondary gravity waves and TIDs with a wavelength of sev-
312 eral hundred to thousand kilometers can be triggered by troposphere convection and de-
313 tected at ionospheric heights. The deep convection activity shown here occurred in the
314 local afternoon and continued for several hours, which was during the similar periods and
315 in locations adjacent to where the MSTIDs were observed. Therefore, the combination
316 of these mutually supportive pieces of evidence collectively suggests that convectively
317 induced AGW/TIDs could have seeded the EPBs in this current case.

318 5 Conclusion

319 This paper presents coordinated ground-based and space-borne observational anal-
320 ysis of equatorial plasma bubbles over the South American area on 24 October 2018. The
321 morphological structure and seeding mechanism of the bubbles were analyzed by using
322 multi-instrument measurements, including the GOLD/UV imaging spectrograph, GNSS
323 TEC maps, Swarm in situ electron density data, ionosonde measurements, and cloud tem-
324 perature data. The new observations provided by GOLD/UV geosynchronous images
325 provide a unique tool for studies of plasma irregularity evolution and equatorial iono-
326 spheric dynamics from a fixed longitude location. Furthermore, a combination of differ-
327 ent measurements provides a powerful tool for the space weather community to achieve

328 a more integrated and detailed view on plasma irregularity structure. The main results
329 can be summarized as follows: (1) The plasma depletion developed westward-tilted struc-
330 ture of 10° – 15° relative to the Earth's magnetic field line, with an eastward drift veloc-
331 ity of 80–120 m/s near the magnetic equator that gradually decreased with increasing
332 altitude/latitude. (2) Wave-like oscillations of travelling ionospheric disturbances were
333 observed both in ionosonde electron density profiles and detrended TEC keograms. Ob-
334 served wavelengths were consistent with inter-bubble distances of 500–800 km. (3) At-
335 mospheric gravity waves originating from the tropospheric convective zone are suggested
336 to be a possible seeding process for the development of this EPBs event.

Author Manuscript

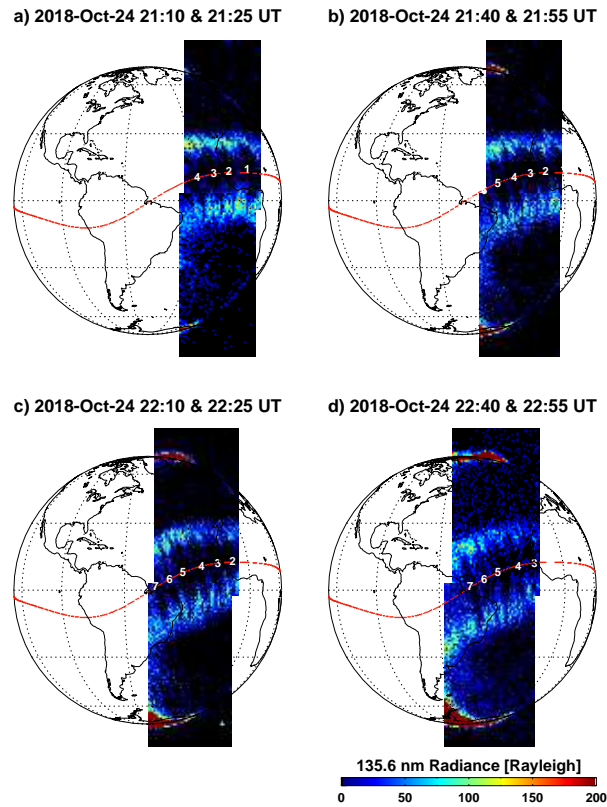


Figure 1. OI 135.6 nm radiance maps observed in successive disk scan of GOLD/UV night-time imaging during 21:10–22:55 UT on 24 October 2018. The dark streaks marked by different numbers represent the optical signature of EPBs. The geomagnetic equator is also shown by red dashed lines. GOLD = Global-Scale Observations of the Limb and Disk; UV = ultraviolet; EPBs = equatorial plasma bubbles.

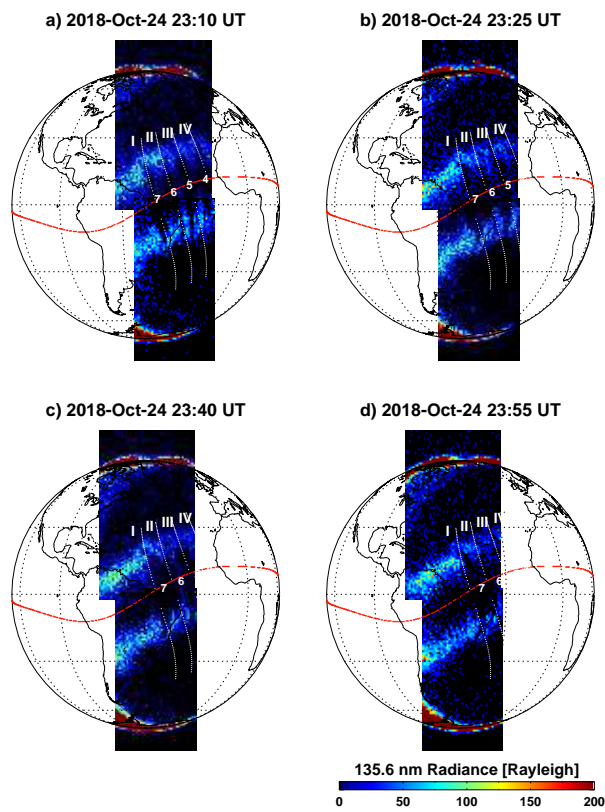


Figure 2. The same as Figure 1, but during the time interval of 23:10–23:55 UT on 24 October 2018. The white dotted curves show 4 different geomagnetic field lines that go across the EPBs. EPBs = equatorial plasma bubbles.

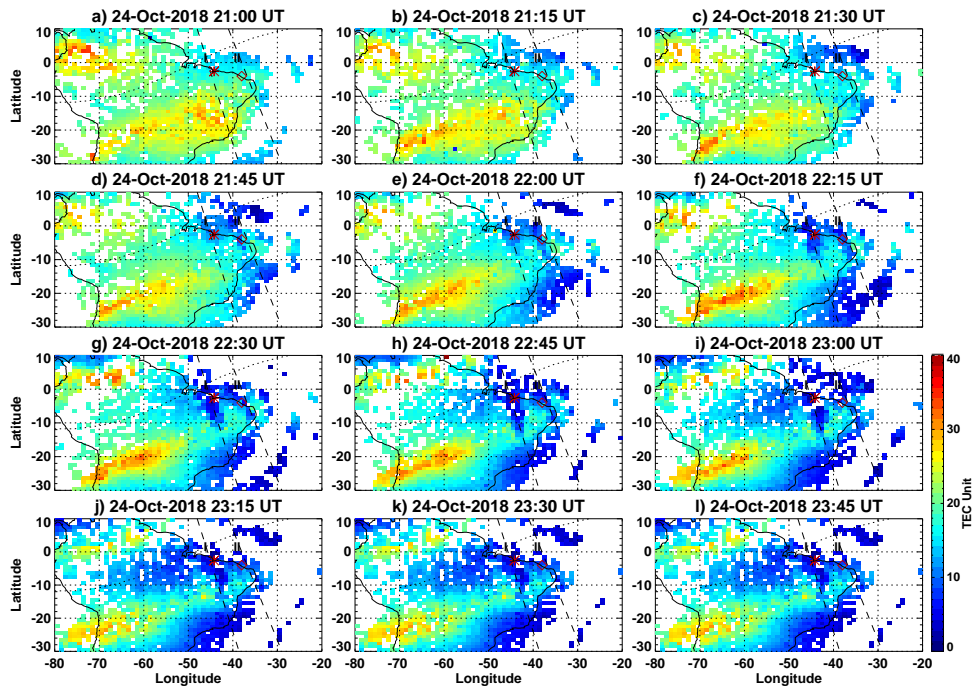


Figure 3. Gridded TEC maps over South American regions with 15-min interval during 21:00–23:45 UT on 24 October 2018. The ionosonde stations of Sao Luis and Fortaleza are marked with asterisk and diamond, respectively. Two geomagnetic field lines (“I” and “II”) that go across the EPBs are marked in dashed lines, and the geomagnetic equator is shown in dotted line. EPBs = equatorial plasma bubbles.

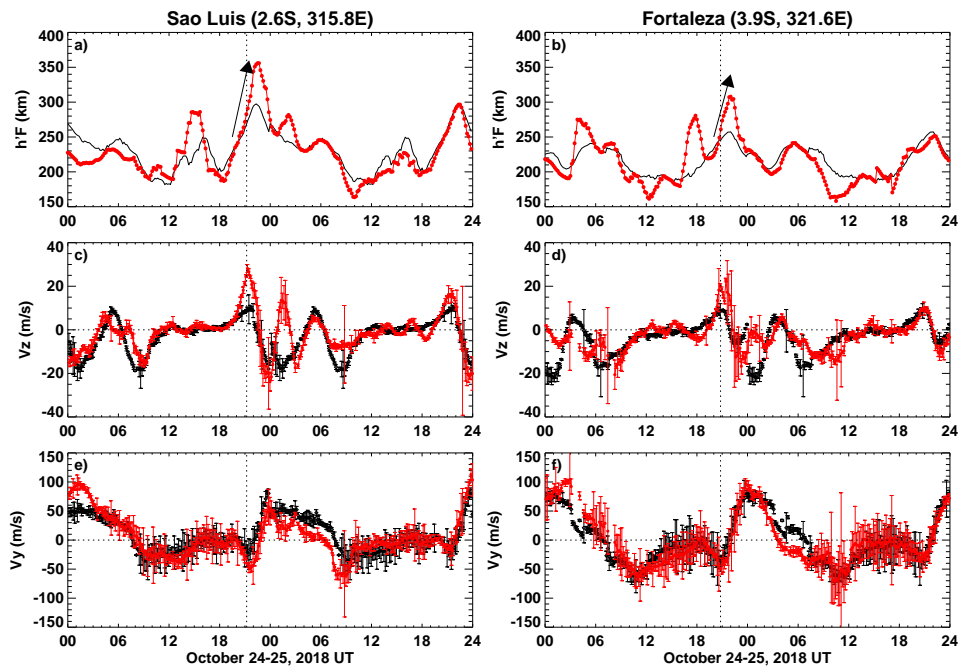


Figure 4. The temporal variation of ionospheric $h'F$, F layer vertical drift, and zonal drift velocity observed at Sao Luis (left panels) and Fortaleza (right panels) during the period of 24–25 October 2018. The black lines represent the values of previous 5-day average. The vertical dotted line represents the local sunset. The error bars represent the velocity spread.

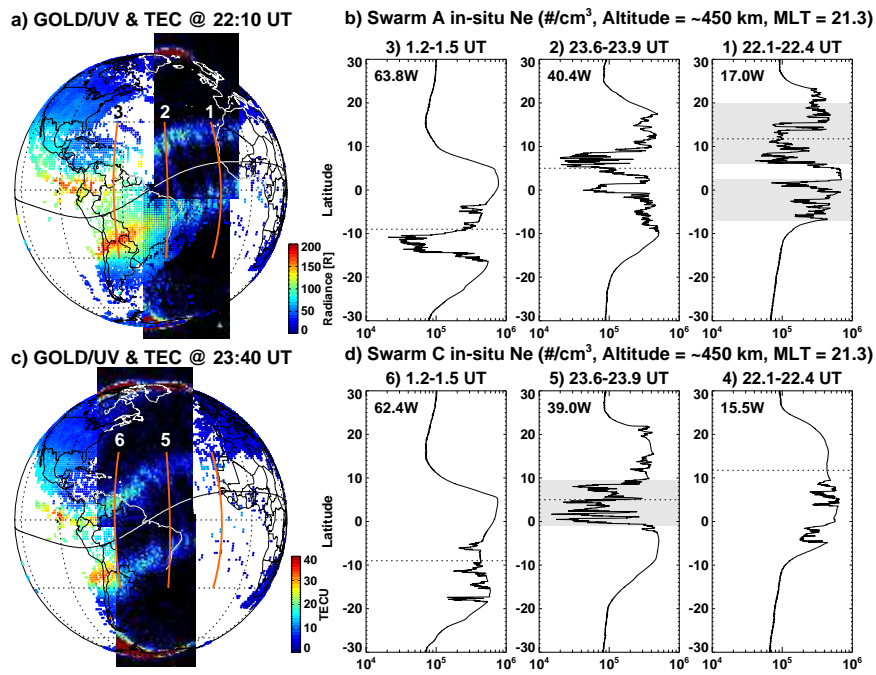


Figure 5. (a) Combined global map of GNSS TEC and OI 135.6 nm radiance of GOLD/UV imaging at 22:10 UT with three consecutive satellite paths of Swarm A. (b) Variation of in situ electron density as a function of latitudes along these paths. (c, d) The same as Figures 5a and 5b, respectively, but at 23:40 UT and for Swarm C satellite paths. The shaded areas represent certain plasma depletions. The magnetic equator is marked by solid line in left panels and dotted line in right panels. GNSS = global navigation satellite system; TEC = total electron content; GOLD = Global-Scale Observations of the Limb and Disk; UV = ultraviolet.

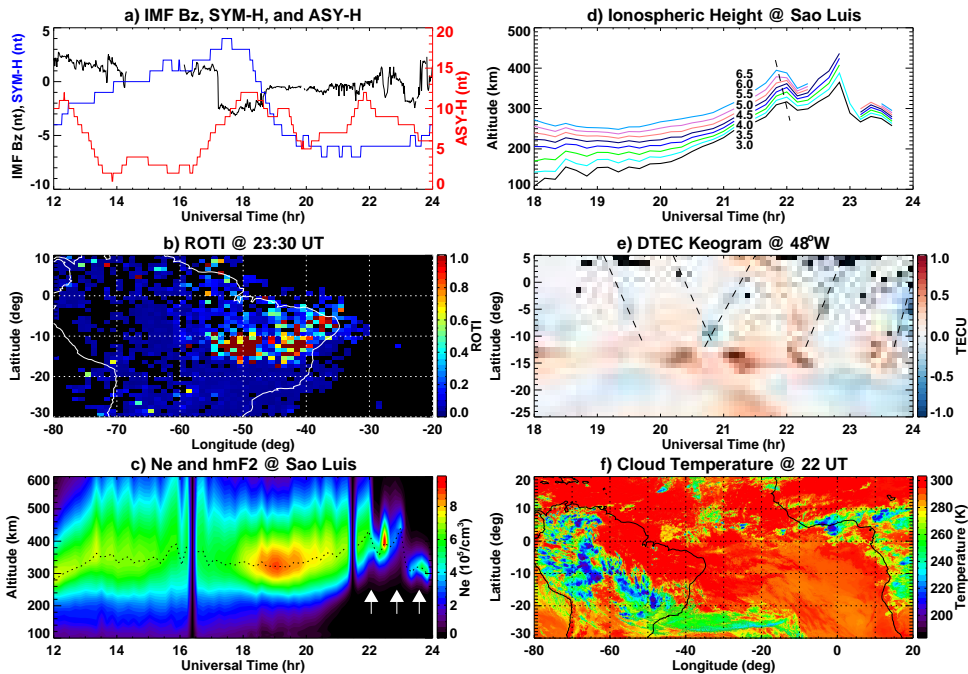


Figure 6. (a) Temporal variation of interplanetary magnetic field (IMF) Bz, the longitudinal asymmetric index (ASY-H), and the symmetric index (SYM-H) between 12 and 24 UT. (b) Rate of TEC Index plot at 23:30 UT. (c) Electron density profile and hmF2 at Sao Luis between 12 and 24 UT. Three quasi-periodic wave-like structures are marked by arrows. (d) Variation of F-layer true heights for different frequencies (3.0–6.5 MHz) at Sao Luis. (e) Keogram plot of detrended total electron content (TEC) as a function of latitude and time at 48°W longitude between 18 and 24 UT. The TID structures are marked by dashed lines. (f) Observation of deep clouds in brightness temperature at 22 UT. All six images are for 24 October 2018.

Acknowledgments

We greatly appreciate NASA/GOLD mission science team for providing data to the public (gold.cs.ucf.edu). We acknowledge ESA for providing the SWARM data (<http://earth.esa.int/swarm>). GPS TEC data products and access through the Madrigal distributed data system are provided to the community (<http://cedar.openmadrigal.org/>) by the Massachusetts Institute of Technology (MIT) under support from US National Science Foundation grant AGS-1762141. S. Zou acknowledges NASA 80NSSC20K0190 for the support of this work. AJC and SRZ acknowledge the ONR grant N00014-17-1-2186, and SRZ and AJC acknowledge the AFOSR MURI grant FA9559-16-1-0364. Data for the TEC processing is provided from the following organizations: The Crustal Dynamics Data Information System (CDDIS), the Scripps Orbit and Permanent Array Center (SOPAC), the Continuously Operating Reference System (CORS), the EUREF Permanent GNSS network (EPN), the University NAVSTAR Consortium (UNAVCO), Institut Geographique National in France (IGN), the Brazilian Network for Continuous Monitoring (RBMC), National Geodetic Survey, Instituto Brasileiro de Geografia e Estatística, RAMSAC CORS of Instituto Geográfico Nacional de la República Argentina, Arecibo Observatory, Low-Latitude Ionospheric Sensor Network (LISN), Topcon Positioning Systems, Inc., Canadian High Arctic Ionospheric Network, Centro di Ricerche Sismologiche, Système d’Observation du Niveau des Eaux Littorales (SONEL), RENAG : REseau National GPS permanent, GeoNet - the official source of geological hazard information for New Zealand, GNSS Reference Networks, Finnish Meteorological Institute, and SWEPOS - Sweden. The IMF, ASY-H, and SYM-H data are obtained from NASA/GSFCs Space Physics Data Facilities OM-

359 NIWeb service (<https://cdaweb.gsfc.nasa.gov/>). We acknowledge the University of Mas-
 360 sachusetts Lowell for providing ionosonde data from the DIDB database of Global Iono-
 361 spheric Radio Observatory (<http://giro.uml.edu/>). The Cloud brightness temperature
 362 (BT) data was provided by the National Aeronautics and Space Administration (NASA)
 363 Goddard Earth Sciences Data and Information Services Central (<https://disc.gsfc.nasa.gov/>).

364 References

- 365 Aa, E., Huang, W., Liu, S., Ridley, A., Zou, S., Shi, L., ... Wang, T. (2018).
 366 Midlatitude Plasma Bubbles Over China and Adjacent Areas During a
 367 Magnetic Storm on 8 September 2017. *Space Weather*, *16*, 321-331. doi:
 368 10.1002/2017SW001776
- 369 Aa, E., Zou, S., Ridley, A. J., Zhang, S.-R., Coster, A. J., Erickson, P. J., ... Ren,
 370 J. (2019). Merging of storm-time midlatitude traveling ionospheric distur-
 371 bances and equatorial plasma bubbles. *Space Weather*, *17*, 285-298. doi:
 372 10.1029/2018SW002101
- 373 Abdu, M. A. (2005). Equatorial ionosphere thermosphere system: Electrodynamic
 374 ics and irregularities. *Adv. Space Res.*, *35*, 771-787. doi: 10.1016/j.asr.2005.03
 375 .150
- 376 Abdu, M. A. (2012). Equatorial spread F/plasma bubble irregularities under storm
 377 time disturbance electric fields. *J. Atmos. Terr. Phys.*, *75*, 44-56. doi: 10.1016/
 378 j.jastp.2011.04.024
- 379 Abdu, M. A., Alam Kherani, E., Batista, I. S., de Paula, E. R., Fritts, D. C., & So-
 380 bral, J. H. A. (2009). Gravity wave initiation of equatorial spread F/plasma
 381 bubble irregularities based on observational data from the SpreadFEx cam-
 382 paign. *Annales Geophysicae*, *27*, 2607-2622. doi: 10.5194/angeo-27-2607-2009
- 383 Abdu, M. A., Batista, I. S., Takahashi, H., MacDougall, J., Sobral, J. H., Medeiros,
 384 A. F., & Trivedi, N. B. (2003). Magnetospheric disturbance induced equatorial
 385 plasma bubble development and dynamics: A case study in Brazilian sector. *J.*
 386 *Geophys. Res.*, *108*, 1449. doi: 10.1029/2002JA009721
- 387 Ajith, K. K., Ram, S. T., Yamamoto, M., Yokoyama, T., Gowtam, V. S., Otsuka,
 388 Y., ... Niranjan, K. (2015). Explicit characteristics of evolutionary-type
 389 plasma bubbles observed from Equatorial Atmosphere Radar during the low
 390 to moderate solar activity years 2010-2012. *Journal of Geophysical Research*
 391 *Space Physics*, *120*, 1371-1382. doi: 10.1002/2014JA020878
- 392 Azeem, I., Yue, J., Hoffmann, L., Miller, S. D., Straka, W. C., & Crowley, G. (2015).
 393 Multisensor profiling of a concentric gravity wave event propagating from the
 394 troposphere to the ionosphere. *Geophysical Research Letters*, *42*, 7874-7880.
 395 doi: 10.1002/2015GL065903
- 396 Barros, D., Takahashi, H., Wrasse, C. M., & Figueiredo, C. A. O. B. (2018). Charac-
 397 teristics of equatorial plasma bubbles observed by TEC map based on ground-
 398 based GNSS receivers over South America. *Annales Geophysicae*, *36*, 91-100.
 399 doi: 10.5194/angeo-36-91-2018
- 400 Basu, S., Basu, S., Rich, F. J., Groves, K. M., MacKenzie, E., Coker, C., ... Becker-
 401 Guedes, F. (2007). Response of the equatorial ionosphere at dusk to pene-
 402 tration electric fields during intense magnetic storms. *J. Geophys. Res.*, *112*,
 403 A08308. doi: 10.1029/2006JA012192
- 404 Buhari, S. M., Abdullah, M., Hasbi, A. M., Otsuka, Y., Yokoyama, T., Nishioka, M.,
 405 & Tsugawa, T. (2014). Continuous generation and two-dimensional struc-
 406 ture of equatorial plasma bubbles observed by high-density GPS receivers in
 407 Southeast Asia. *Journal of Geophysical Research Space Physics*, *119*, 10. doi:
 408 10.1002/2014JA020433
- 409 Buhari, S. M., Abdullah, M., Yokoyama, T., Otsuka, Y., Nishioka, M., Hasbi, A. M.,
 410 ... Tsugawa, T. (2017). Climatology of successive equatorial plasma bubbles
 411 observed by GPS ROTI over Malaysia. *Journal of Geophysical Research Space*

- 412 *Physics*, 122, 2174-2184. doi: 10.1002/2016JA023202
- 413 Burke, W., Gentile, L. C., Huang, C. Y., Valladares, C. E., & Su, S. Y. (2004).
414 Longitudinal variability of equatorial plasma bubbles observed by DMSP and
415 ROCSAT-1. *J. Geophys. Res.*, 109, A12301. doi: 10.1029/2004JA010583
- 416 Burke, W., Huang, C., Gentile, L., & Bauer, L. (2004). Seasonal-longitudinal vari-
417 ability of equatorial plasma bubbles. *Annales Geophysicae*, 22, 3089-3098. doi:
418 10.5194/angeo-22-3089-2004
- 419 Carter, B. A., Zhang, K., Norman, R., Kumar, V. V., & Kumar, S. (2013). On the
420 occurrence of equatorial F-region irregularities during solar minimum using ra-
421 dio occultation measurements. *J. Geophys. Res. Space Physics*, 118, 892-904.
422 doi: 10.1002/jgra.50089
- 423 Chapagain, N. P., Makela, J. J., Meriwether, J. W., Fisher, D. J., Buriti, R. A., &
424 Medeiros, A. F. (2012). Comparison of nighttime zonal neutral winds and
425 equatorial plasma bubble drift velocities over Brazil. *Journal of Geophysical*
426 *Research Space Physics*, 117, A06309. doi: 10.1029/2012JA017620
- 427 Cherniak, I., Krankowski, A., & Zakharenkova, I. (2014). Observation of the iono-
428 spheric irregularities over the Northern Hemisphere: Methodology and service.
429 *Radio Sci.*, 49, 653-662. doi: 10.1002/2014RS005433
- 430 Cherniak, I., & Zakharenkova, I. (2016). First observations of super plasma bubbles
431 in Europe. *Geophys. Res. Lett.*, 43, 11. doi: 10.1002/2016GL071421
- 432 Cherniak, I., Zakharenkova, I., & Sokolovsky, S. (2019). Multi-instrumental obser-
433 vation of storm-induced ionospheric plasma bubbles at equatorial and middle
434 latitudes. *Journal of Geophysical Research: Space Physics*, 124, 1491-1508.
435 doi: 10.1029/2018JA026309
- 436 Comberiate, J., & Paxton, L. J. (2010). Coordinated UV imaging of equatorial
437 plasma bubbles using TIMED/GUVI and DMSP/SSUSI. *Space Weather*, 8,
438 S10002. doi: 10.1029/2009SW000546
- 439 Coster, A. J., Goncharenko, L., Zhang, S.-R., Erickson, P. J., Rideout, W., & Vier-
440 inen, J. (2017). GNSS Observations of Ionospheric Variations During the
441 21 August 2017 Solar Eclipse. *Geophysical Research Letters*, 44, 12. doi:
442 10.1002/2017GL075774
- 443 Eastes, R. W., McClintock, W. E., Burns, A. G., Anderson, D. N., Andersson, L.,
444 Codrescu, M., ... Oberheide, J. (2017). The Global-Scale Observations of the
445 Limb and Disk (GOLD) Mission. *Space Science Reviews*, 212, 383-408. doi:
446 10.1007/s11214-017-0392-2
- 447 Eastes, R. W., Solomon, S. C., Daniell, R. E., Anderson, D. N., Burns, A. G., Eng-
448 land, S. L., ... McClintock, W. E. (2019). Global-scale observations of the
449 equatorial ionization anomaly. *Geophysical Research Letters*, 46(16), 9318-
450 9326. doi: 10.1029/2019GL084199
- 451 Ebihara, Y., & Tanaka, T. (2015). Substorm simulation: Insight into the mecha-
452 nisms of initial brightening. *J. Geophys. Res. Space Physics*, 120, 7270-7288.
453 doi: 10.1002/2015JA021516
- 454 Fejer, B. G., Scherliess, L., & de Paula, E. R. (1999). Effects of the vertical plasma
455 drift velocity on the generation and evolution of equatorial spread F. *J. Geo-*
456 *phys. Res.*, 104, 19859-19870. doi: 10.1029/1999JA900271
- 457 Gurav, O. B., Sharma, A. K., Ghodpage, R. N., Nade, D. P., Chavan, G. A., Gaik-
458 wad, H. P., & Patil, P. T. (2018). Zonal Drift Velocity of Equatorial Plasma
459 Bubbles During Ascending Phase of 24th Solar Cycle Using All-Sky Imager
460 Over Kolhapur, India. *Journal of Geophysical Research Space Physics*, 123,
461 10. doi: 10.1029/2018JA025810
- 462 Hickey, D. A., Martinis, C. R., Mendillo, M., Baumgardner, J., Wroten, J., & Milla,
463 M. (2018). Simultaneous 6300 Å airglow and radar observations of ionospheric
464 irregularities and dynamics at the geomagnetic equator. *Annales Geophysicae*,
465 36(2), 473-487. doi: 10.5194/angeo-36-473-2018
- 466 Hoffmann, L., & Alexander, M. J. (2010). Occurrence frequency of convective

- 467 gravity waves during the North American thunderstorm season. *Journal of*
 468 *Geophysical Research Atmospheres*, *115*, D20111. doi: 10.1029/2010JD014401
- 469 Huang, C.-S., de La Beaujardiere, O., Pfaff, R. F., Retterer, J. M., Roddy, P. A.,
 470 Hunton, D. E., ... Rich, F. J. (2010). Zonal drift of plasma particles inside
 471 equatorial plasma bubbles and its relation to the zonal drift of the bubble
 472 structure. *Journal of Geophysical Research Space Physics*, *115*, A07316. doi:
 473 10.1029/2010JA015324
- 474 Huang, C.-S., La Beaujardiere, O., Roddy, P. A., Hunton, D. E., Liu, J. Y., & Chen,
 475 S. P. (2014). Occurrence probability and amplitude of equatorial ionospheric
 476 irregularities associated with plasma bubbles during low and moderate solar
 477 activities (2008-2012). *J. Geophys. Res. Space Physics*, *119*, 1186-1199. doi:
 478 10.1002/2013JA019212
- 479 Huang, C. Y., Burke, W. J., Machuzak, J. S., Gentile, L. C., & Sultan, P. J. (2002).
 480 Equatorial plasma bubbles observed by DMSP satellites during a full solar
 481 cycle: Toward a global climatology. *J. Geophys. Res.*, *107*, 1434. doi:
 482 10.1029/2002JA009452
- 483 Huba, J. D., Ossakow, S. L., Joyce, G., Krall, J., & England, S. L. (2009). Three-
 484 dimensional equatorial spread F modeling: Zonal neutral wind effects. *Geo-*
 485 *physical Research Letters*, *36*, L19106. doi: 10.1029/2009GL040284
- 486 Hysell, D. L. (2000). An overview and synthesis of plasma irregularities in equa-
 487 torial spread F. *Journal of Atmospheric and Solar-Terrestrial Physics*, *62*,
 488 1037-1056. doi: 10.1016/S1364-6826(00)00095-X
- 489 Hysell, D. L., Kudeki, E., & Chau, J. L. (2005). Possible ionospheric preconditioning
 490 by shear flow leading to equatorial spread F. *Annales Geophysicae*, *23*, 2647-
 491 2655. doi: 10.5194/angeo-23-2647-2005
- 492 Hysell, D. L., Larsen, M. F., Swenson, C. M., & Wheeler, T. F. (2006). Shear flow
 493 effects at the onset of equatorial spread F. *Journal of Geophysical Research*
 494 *Space Physics*, *111*, A11317. doi: 10.1029/2006JA011963
- 495 Janowiak, J., Joyce, B., & Xie, P. (2017). *Ncep/cpc 13 half hourly 4km global (60s -*
 496 *60n) merged ir v1*. NASA Goddard Earth Sciences Data and Information Ser-
 497 vices Center. doi: 10.5067/P4HZB9N27EKU
- 498 Jin, H., Zou, S., Chen, G., Yan, C., Zhang, S., & Yang, G. (2018). Formation
 499 and Evolution of Low-Latitude F Region Field-Aligned Irregularities Dur-
 500 ing the 7-8 September 2017 Storm: Hainan Coherent Scatter Phased Ar-
 501 ray Radar and Digisonde Observations. *Space Weather*, *16*, 648-659. doi:
 502 10.1029/2018SW001865
- 503 Jonah, O. F., Coster, A., Zhang, S., Goncharenko, L., Erickson, P. J., de Paula,
 504 E. R., & Kherani, E. A. (2018). TID Observations and Source Analysis
 505 During the 2017 Memorial Day Weekend Geomagnetic Storm Over North
 506 America. *Journal of Geophysical Research Space Physics*, *123*, 8749-8765. doi:
 507 10.1029/2018JA025367
- 508 Katamzi-Joseph, Z. T., Habarulema, J. B., & Hernández-Pajares, M. (2017).
 509 Midlatitude postsunset plasma bubbles observed over Europe during intense
 510 storms in April 2000 and 2001. *Space Weather*, *15*(9), 1177-1190. doi:
 511 10.1002/2017SW001674
- 512 Kelley, M. C., Makela, J. J., Paxton, L. J., Kamalabadi, F., Comberiate, J. M., &
 513 Kil, H. (2003). The first coordinated ground- and space-based optical ob-
 514 servations of equatorial plasma bubbles. *Geophys. Res. Lett.*, *30*, 1766. doi:
 515 10.1029/2003GL017301
- 516 Kil, H. (2015). The Morphology of Equatorial Plasma Bubbles - a review. *J. Astron.*
 517 *Space Sci.*, *32*, 13-19. doi: 10.5140/JASS.2015.32.1.13
- 518 Kil, H., Heelis, R. A., Paxton, L. J., & Oh, S.-J. (2009). Formation of a plasma de-
 519 pletion shell in the equatorial ionosphere. *J. Geophys. Res.*, *114*, A11302. doi:
 520 10.1029/2009JA014369
- 521 Kil, H., Kintner, P. M., de Paula, E. R., & Kantor, I. J. (2002). Latitudinal varia-

- tions of scintillation activity and zonal plasma drifts in South America. *Radio Science*, *37*, 1006. doi: 10.1029/2001RS002468
- Kil, H., Su, S.-Y., Paxton, L. J., Wolven, B. C., Zhang, Y., Morrison, D., & Yeh, H. C. (2004). Coincident equatorial bubble detection by TIMED/GUVI and ROCSAT-1. *Geophys. Res. Letts*, *31*, L03809. doi: 10.1029/2003GL018696
- Krall, J., Huba, J. D., Ossakow, S. L., Joyce, G., Makela, J. J., Miller, E. S., & Kelley, M. C. (2011). Modeling of equatorial plasma bubbles triggered by non-equatorial traveling ionospheric disturbances. *Geophys. Res. Lett.*, *38*, L08103. doi: 10.1029/2011GL046890
- Kudeki, E., Akgiray, A., Milla, M., Chau, J. L., & Hysell, D. L. (2007). Equatorial spread-F initiation: Post-sunset vortex, thermospheric winds, gravity waves. *Journal of Atmospheric and Solar-Terrestrial Physics*, *69*, 2416-2427. doi: 10.1016/j.jastp.2007.04.012
- Li, G., Ning, B., Abdu, M. A., Otsuka, Y., Yokoyama, T., Yamamoto, M., & Liu, L. (2013). Longitudinal characteristics of spread F backscatter plumes observed with the EAR and Sanya VHF radar in Southeast Asia. *J. Geophys. Res.*, *118*, 6544-6557. doi: 10.1002/jgra.50581
- Li, G., Ning, B., Wang, C., Abdu, M. A., Otsuka, Y., Yamamoto, M., ... Chen, J. (2018). Storm-enhanced development of post-sunset equatorial plasma bubbles around the meridian 120E/60W on 7-8 September 2017. *J. Geophys. Res. Space Physics*, *123*, 1-16. doi: 10.1029/2018JA025871
- Li, G., Otsuka, Y., Ning, B., Abdu, M. A., Yamamoto, M., Wan, W., ... Abadi, P. (2016). Enhanced ionospheric plasma bubble generation in more active ITCZ. *Geophys. Res. Lett.*, *43*, 2389-2395. doi: 10.1002/2016GL068145
- Lühr, H., Xiong, C., Park, J., & Rauberg, J. (2014). Systematic study of intermediate-scale structures of equatorial plasma irregularities in the ionosphere based on CHAMP observations. *Frontiers in Physics*, *2*, 15. doi: 10.3389/fphy.2014.00015
- Ma, G., & Maruyama, T. (2006). A super bubble detected by dense GPS network at east Asian longitudes. *Geophys. Res. Lett.*, *33*, L21103. doi: 10.1029/2006GL027512
- Makela, J. J. (2006). A review of imaging low-latitude ionospheric irregularity processes. *Journal of Atmospheric and Solar-Terrestrial Physics*, *68*, 1441-1458. doi: 10.1016/j.jastp.2005.04.014
- Mandal, S., Pallamraju, D., Karan, D. K., Phadke, K. A., Singh, R. P., & Suryawan-shi, P. (2019). On deriving gravity wave characteristics in the daytime upper atmosphere using radio technique. *Journal of Geophysical Research: Space Physics*, *124*(8), 6985-6997. doi: 10.1029/2019JA026723
- Martinis, C., Baumgardner, J., Mendillo, M., Wroten, J., Coster, A., & Paxton, L. (2015). The night when the auroral and equatorial ionospheres converged. *J. Geophys. Res. Space Physics*, *120*, 8085-8095. doi: 10.1002/2015JA021555
- Martinis, C., Eccles, J. V., Baumgardner, J., Manzano, J., & Mendillo, M. (2003). Latitude dependence of zonal plasma drifts obtained from dual-site airglow observations. *Journal of Geophysical Research Space Physics*, *108*, 1129. doi: 10.1029/2002JA009462
- McClure, J. P., Singh, S., Bamgboye, D. K., Johnson, F. S., & Kil, H. (1998). Occurrence of equatorial F region irregularities: Evidence for tropospheric seeding. *J. Geophys. Res.*, *103*, 29119-29136. doi: 10.1029/98JA02749
- Miller, E. S., Makela, J. J., & Kelley, M. C. (2009). Seeding of equatorial plasma depletions by polarization electric fields from middle latitudes: Experimental evidence. *Geophys. Res. Lett.*, *36*, L18105. doi: 10.1029/2009GL039695
- Nishioka, M., Saito, A., & Tsugawa, T. (2008). Occurrence characteristics of plasma bubble derived from global ground-based GPS receiver networks. *J. Geophys. Res.*, *113*, A05301. doi: 10.1029/2007JA012605
- Otsuka, Y., Shiokawa, K., Ogawa, T., & Wilkinson, P. (2002). Geomagnetic con-

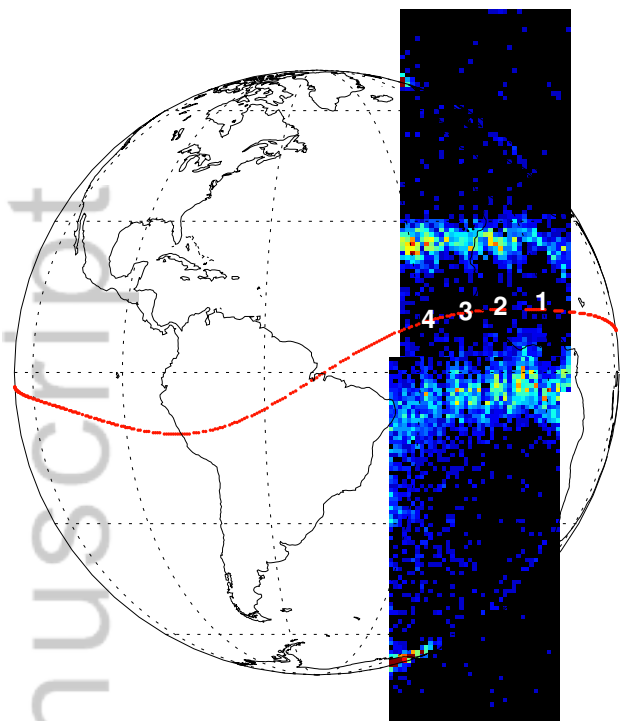
- 577 jugate observations of equatorial airglow depletions. *Geophys. Res. Lett.*, *29*,
578 1753. doi: 10.1029/2002GL015347
- 579 Perkins, F. (1973). Spread F and ionospheric currents. *J. Geophys. Res.*, *78*, 218-
580 226. doi: 10.1029/JA078i001p00218
- 581 Pimenta, A. A., Fagundes, P. R., Sahai, Y., Bittencourt, J. A., & Abalde, J. R.
582 (2003). Equatorial F-region plasma depletion drifts: latitudinal and sea-
583 sonal variations. *Annales Geophysicae*, *21*, 2315-2322. doi: 10.5194/
584 angeo-21-2315-2003
- 585 Reinisch, B. W., & Huang, X. (2001). Deducing topside profiles and total electron
586 content from bottomside ionograms. *Advances in Space Research*, *27*, 23-30.
587 doi: 10.1016/S0273-1177(00)00136-8
- 588 Retterer, J. M. (2010, Mar). Forecasting low-latitude radio scintillation with 3-D
589 ionospheric plume models: 1. Plume model. *Journal of Geophysical Research: Space Physics*, *115*(A3), A03306. doi: 10.1029/2008JA013839
- 590 Retterer, J. M., & Roddy, P. (2014, May). Faith in a seed: on the origins of equa-
591 torial plasma bubbles. *Ann. Geophys.*, *32*, 485-498. doi: 10.5194/angeo-32-485-
592 -2014
- 593 Rideout, W., & Coster, A. (2006). Automated gps processing for global total elec-
594 tron content data. *GPS Solut.*, *10*(3), 219-228. doi: 10.1007/s10291-006-0029
595 -5
- 596 Rishbeth, H. (1997). The ionospheric E-layer and F-layer dynamos - a tutorial
597 review. *Journal of Atmospheric and Solar-Terrestrial Physics*, *59*, 1873-1880.
598 doi: 10.1016/S1364-6826(97)00005-9
- 599 Rodrigues, F. S., Hickey, D. A., Zhan, W., Martinis, C. R., Fejer, B. G., Milla,
600 M. A., & Arratia, J. F. (2018). Multi-instrumented observations of
601 the equatorial F-region during June solstice: large-scale wave structures
602 and spread-F. *Progress in Earth and Planetary Science*, *5*, 14. doi:
603 10.1186/s40645-018-0170-0
- 604 Shiokawa, K., Otsuka, Y., Lynn, K. J., Wilkinson, P., & Tsugawa, T. (2015).
605 Airglow-imaging observation of plasma bubble disappearance at geomag-
606 netically conjugate points. *Earth Planets Space*, *67*, 43. doi: 10.1186/
607 s40623-015-0202-6
- 608 Smith, J., & Heelis, R. A. (2017). Equatorial plasma bubbles: Variations of oc-
609 currence and spatial scale in local time, longitude, season, and solar activity. *J.*
610 *Geophys. Res. Space Physics*, *122*, 5743-5755. doi: 10.1002/2017JA024128
- 611 Sun, L., Xu, J., Wang, W., Yuan, W., Li, Q., & Jiang, C. (2016). A statistical anal-
612 ysis of equatorial plasma bubble structures based on an all-sky airglow imager
613 network in China. *Journal of Geophysical Research Space Physics*, *121*, 11.
614 doi: 10.1002/2016JA022950
- 615 Takahashi, H., Wrasse, C. M., Otsuka, Y., Ivo, A., Gomes, V., Paulino, I., ... Sh-
616 iokawa, K. (2015). Plasma bubble monitoring by TEC map and 630 nm
617 airglow image. *Journal of Atmospheric and Solar-Terrestrial Physics*, *130*,
618 151-158. doi: 10.1016/j.jastp.2015.06.003
- 619 Taori, A., Parihar, N., Ghodpage, R., Dashora, N., Sripathi, S., Kherani, E. A., &
620 Patil, P. T. (2015). Probing the possible trigger mechanisms of an equatorial
621 plasma bubble event based on multistation optical data. *J. Geophys. Res.*
622 *Space Physics*, *120*, 8835-8847. doi: 10.1002/2015JA021541
- 623 Tsunoda, R. T. (2010). On equatorial spread F: Establishing a seeding hypoth-
624 esis. *Journal of Geophysical Research Space Physics*, *115*, A12303. doi: 10
625 .1029/2010JA015564
- 626 Tsunoda, R. T. (2015). Upwelling: a unit of disturbance in equatorial spread F.
627 *Progress in Earth and Planetary Science*, *2*, 9. doi: 10.1186/s40645-015-0038
628 -5
- 629 Tsunoda, R. T., Livingston, R. C., McClure, J. P., & Hanson, W. B. (1982). Equa-
630 torial plasma bubbles - Vertically elongated wedges from the bottomside F
631

- 632 layer. *J. Geophys. Res.*, *87*, 9171-9180. doi: 10.1029/JA087iA11p09171
- 633 Tsunoda, R. T., Yamamoto, M., Tsugawa, T., Hoang, T. L., Tulasi Ram, S.,
- 634 Thampi, S. V., . . . Nagatsuma, T. (2011). On seeding, large-scale wave
- 635 structure, equatorial spread F, and scintillations over Vietnam. *Geophys. Res.*
- 636 *Let.*, *38*, L20102. doi: 10.1029/2011GL049173
- 637 Tulasi Ram, S., Ajith, K. K., Yokoyama, T., Yamamoto, M., & Niranjana, K.
- 638 (2017). Vertical rise velocity of equatorial plasma bubbles estimated from
- 639 Equatorial Atmosphere Radar (EAR) observations and HIRB model simula-
- 640 tions. *Journal of Geophysical Research Space Physics*, *122*, 6584-6594. doi:
- 641 10.1002/2017JA024260
- 642 Tulasi Ram, S., Rama Rao, P. V. S., Prasad, D. S. V. V. D., Niranjana, K., Gopi Kr-
- 643 ishna, S., Sridharan, R., & Ravindran, S. (2008, July). Local time dependent
- 644 response of postsunset ESF during geomagnetic storms. *J. Geophys. Res.*, *113*,
- 645 A07310. doi: 10.1029/2007JA012922
- 646 Tulasi Ram, S., Yamamoto, M., Tsunoda, R. T., Chau, H. D., Hoang, T. L., Dantie,
- 647 B., . . . Tsugawa, T. (2014). Characteristics of large-scale wave structure ob-
- 648 served from African and Southeast Asian longitudinal sectors. *J. Geophys.*
- 649 *Res. Space Physics*, *119*, 2288-2297. doi: 10.1002/2013JA019712
- 650 Vadas, S. L. (2007). Horizontal and vertical propagation and dissipation of grav-
- 651 ity waves in the thermosphere from lower atmospheric and thermospheric
- 652 sources. *Journal of Geophysical Research Space Physics*, *112*, A06305. doi:
- 653 10.1029/2006JA011845
- 654 Vadas, S. L., & Liu, H.-l. (2009). Generation of large-scale gravity waves and neutral
- 655 winds in the thermosphere from the dissipation of convectively generated grav-
- 656 ity waves. *Journal of Geophysical Research Space Physics*, *114*, A10310. doi:
- 657 10.1029/2009JA014108
- 658 Valladares, C. E., & Sheehan, R. (2016). Observations of conjugate MSTIDs us-
- 659 ing networks of GPS receivers in the American sector. *Radio Science*, *51*,
- 660 1470-1488. doi: 10.1002/2016RS005967
- 661 Vierinen, J., Coster, A. J., Rideout, W. C., Erickson, P. J., & Norberg, J. (2016).
- 662 Statistical framework for estimating GNSS bias. *Atmospheric Measurement*
- 663 *Techniques*, *9*, 1303-1312. doi: 10.5194/amt-9-1303-2016
- 664 Woodman, R. F., & La Hoz, C. (1976). Radar observations of F region equa-
- 665 torial irregularities. *J. Geophys. Res.*, *81*(31), 5447-5466. doi: 10.1029/
JA081i031p05447
- 667 Xiong, C., Stolle, C., Lühr, H., Park, J., Fejer, B. G., & Kervalishvili, G. N. (2016).
- 668 Scale analysis of equatorial plasma irregularities derived from Swarm constella-
- 669 tion. *Earth, Planets, and Space*, *68*, 121. doi: 10.1186/s40623-016-0502-5
- 670 Yiğit, E., Medvedev, A. S., Aylward, A. D., Ridley, A. J., Harris, M. J., Moldwin,
- 671 M. B., & Hartogh, P. (2012). Dynamical effects of internal gravity waves in
- 672 the equinoctial thermosphere. *Journal of Atmospheric and Solar-Terrestrial*
- 673 *Physics*, *90*, 104-116. doi: 10.1016/j.jastp.2011.11.014
- 674 Yizengaw, E., & Groves, K. M. (2018). Longitudinal and seasonal variability of
- 675 equatorial ionospheric irregularities and electrodynamics. *Space Weather*,
- 676 *16*(8), 946-968. doi: 10.1029/2018SW001980
- 677 Yokoyama, T., & Fukao, S. (2006). Upwelling backscatter plumes in growth phase of
- 678 equatorial spread F observed with the Equatorial Atmosphere Radar. *Geophys.*
- 679 *Res. Let.*, *33*, L08104. doi: 10.1029/2006GL025680
- 680 Zakharenkova, I., Astafyeva, E., & Cherniak, I. (2016, July). GPS and in situ Swarm
- 681 observations of the equatorial plasma density irregularities in the topside iono-
- 682 sphere. *Earth, Planets, and Space*, *68*, 120. doi: 10.1186/s40623-016-0490-5
- 683 Zhang, S.-R., Erickson, P. J., Goncharenko, L. P., Coster, A. J., Rideout, W., &
- 684 Vierinen, J. (2017). Ionospheric Bow Waves and Perturbations Induced by
- 685 the 21 August 2017 Solar Eclipse. *Geophysical Research Letters*, *44*, 12. doi:
- 686 10.1002/2017GL076054

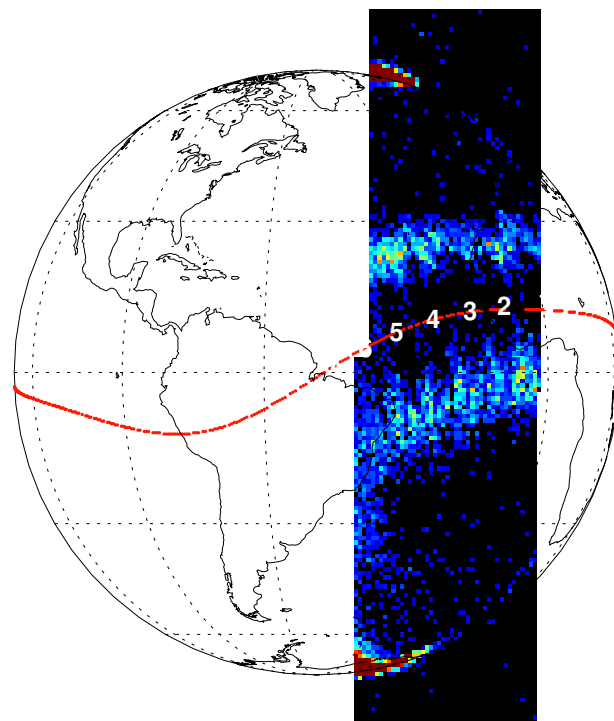
Figure 1.

Author Manuscript

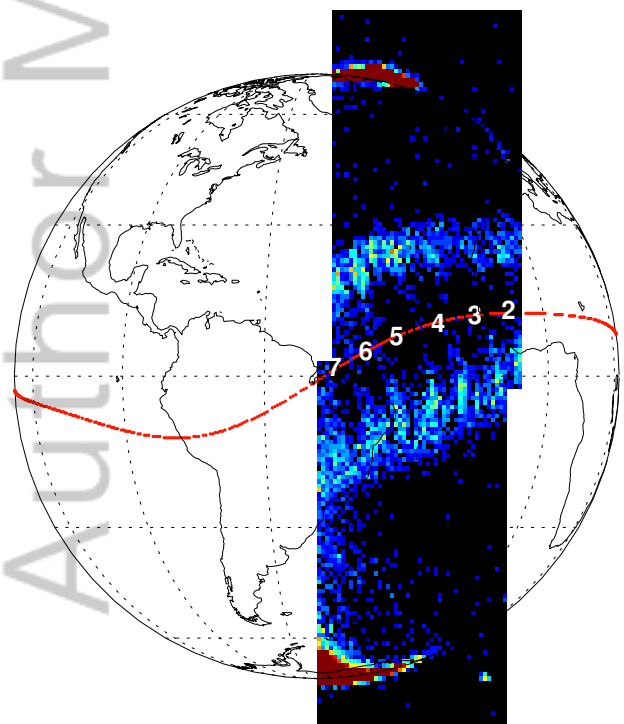
a) 2018-Oct-24 21:10 & 21:25 UT



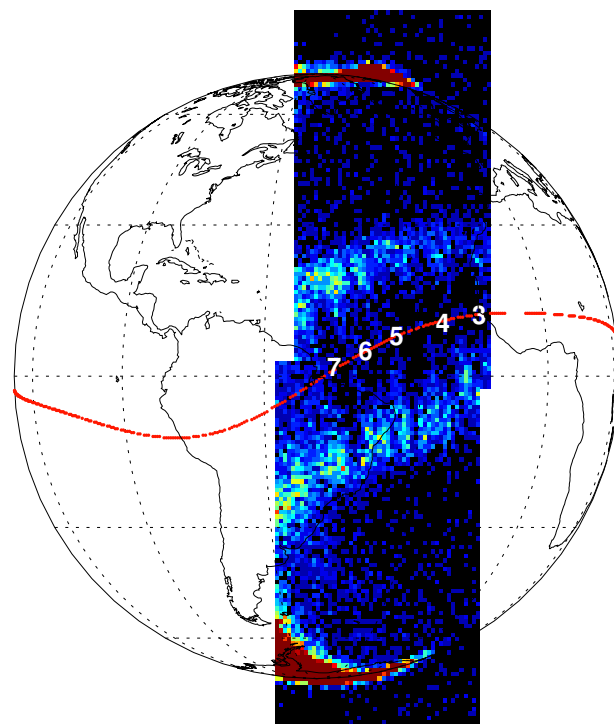
b) 2018-Oct-24 21:40 & 21:55 UT



c) 2018-Oct-24 22:10 & 22:25 UT



d) 2018-Oct-24 22:40 & 22:55 UT



135.6 nm Radiance [Rayleigh]

This article is protected by copyright. All rights reserved.

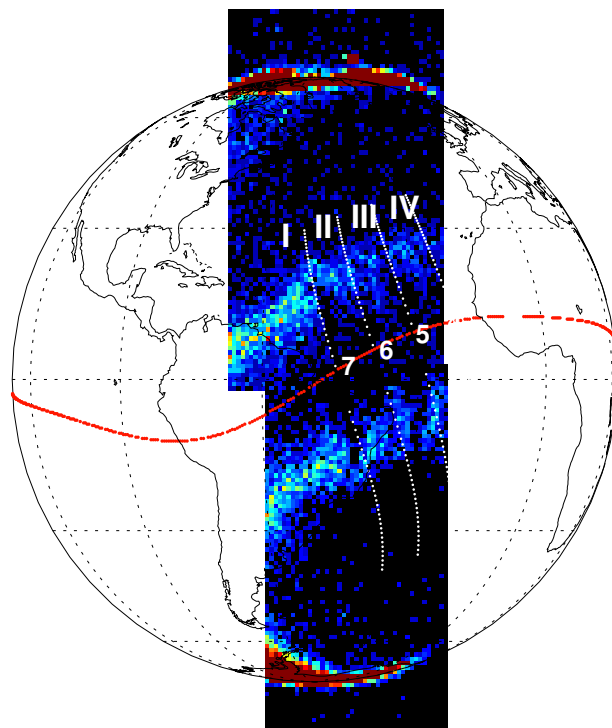
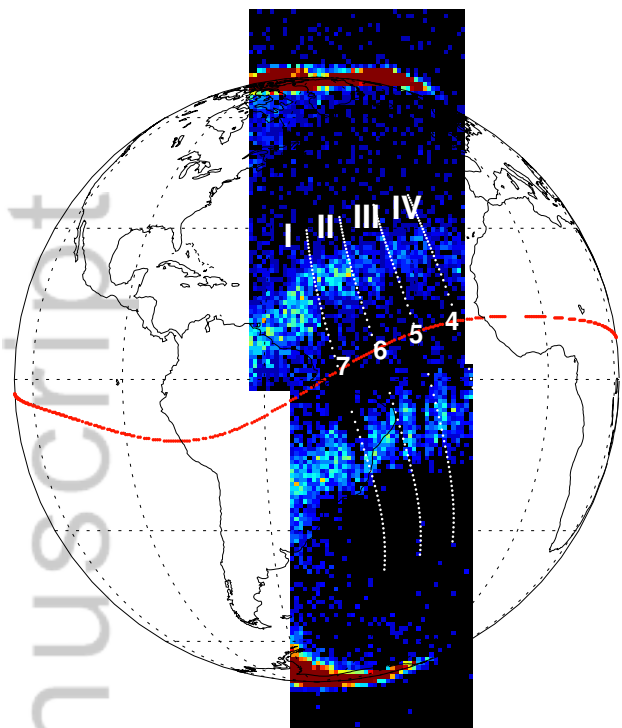
0 50 100 150 200

Figure 2.

Author Manuscript

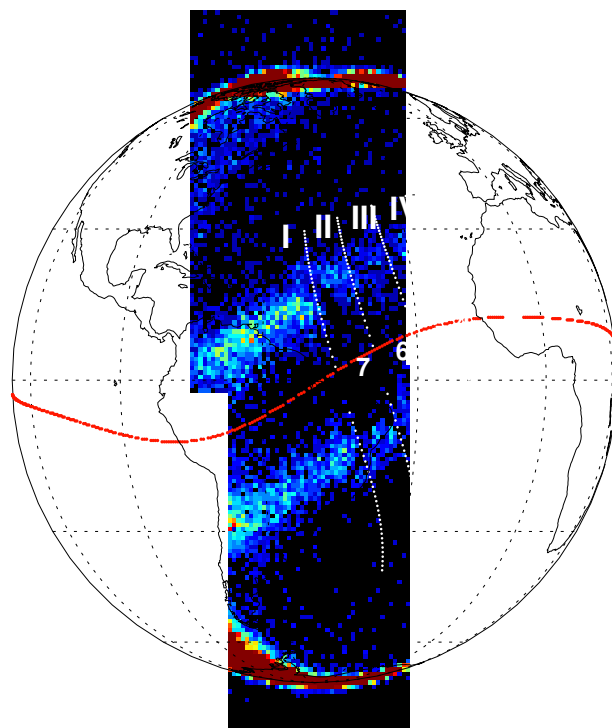
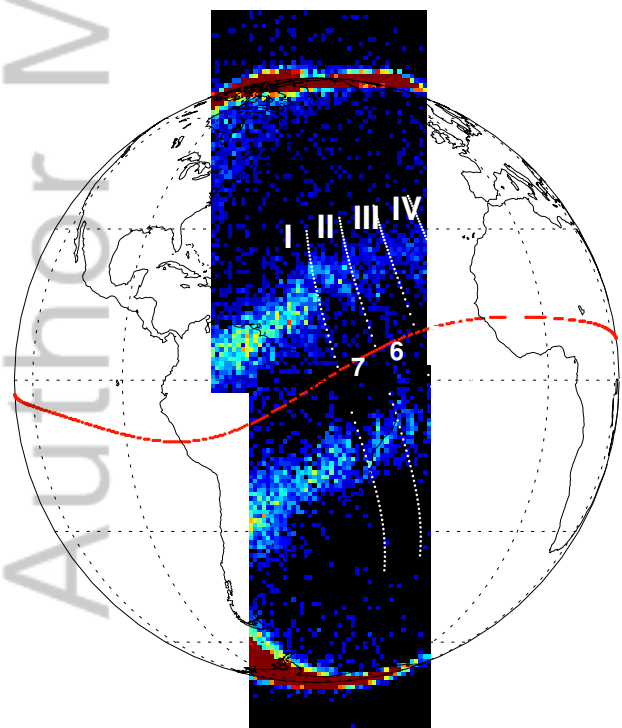
a) 2018-Oct-24 23:10 UT

b) 2018-Oct-24 23:25 UT



c) 2018-Oct-24 23:40 UT

d) 2018-Oct-24 23:55 UT



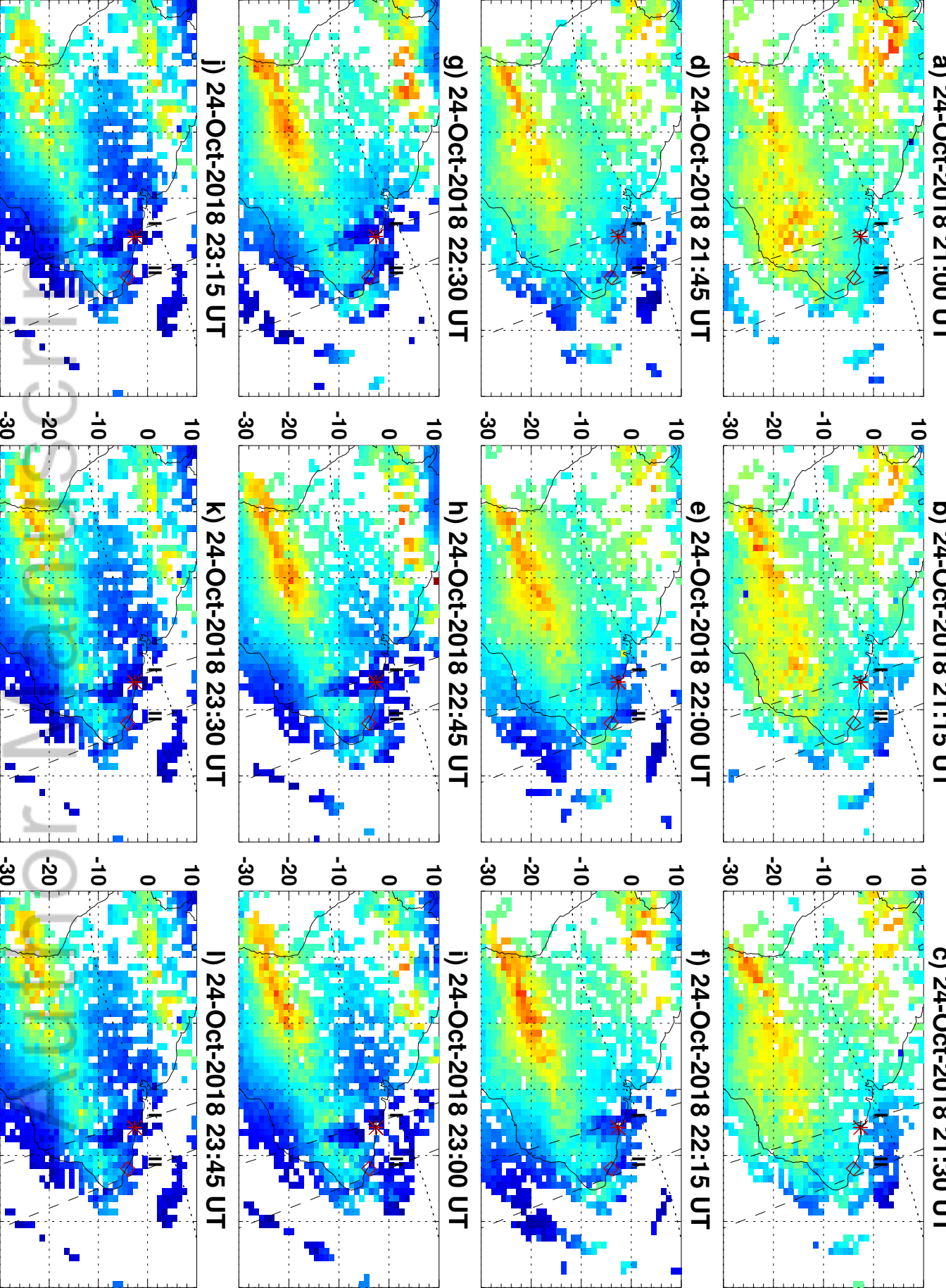
135.6 nm Radiance [Rayleigh]

This article is protected by copyright. All rights reserved.

0 50 100 150 200

Figure 3.

Author Manuscript



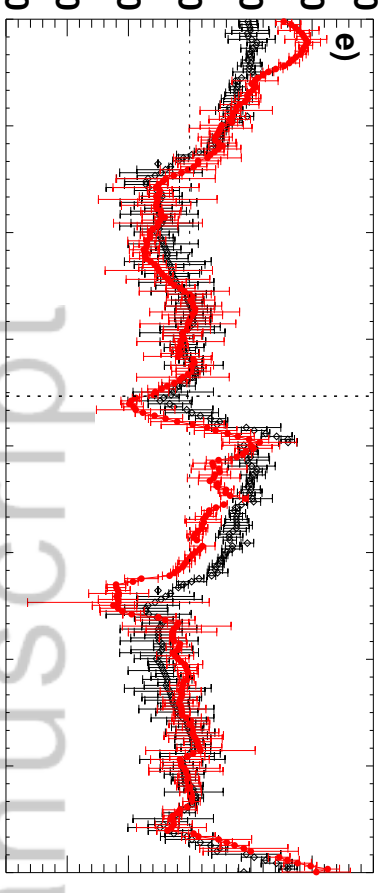
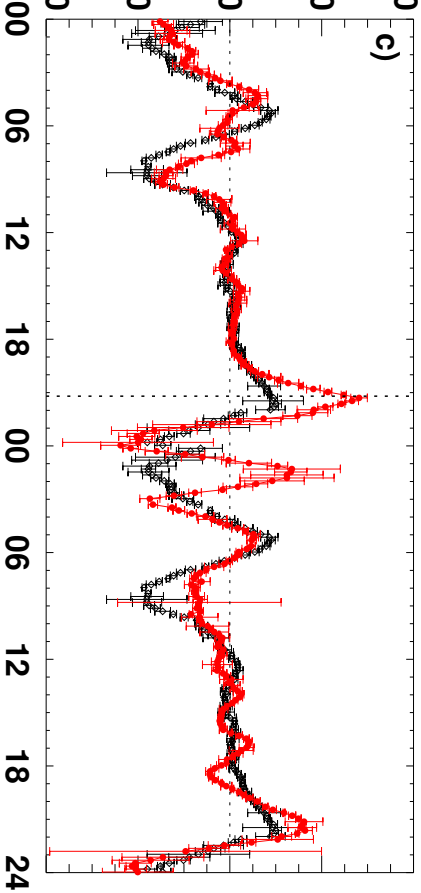
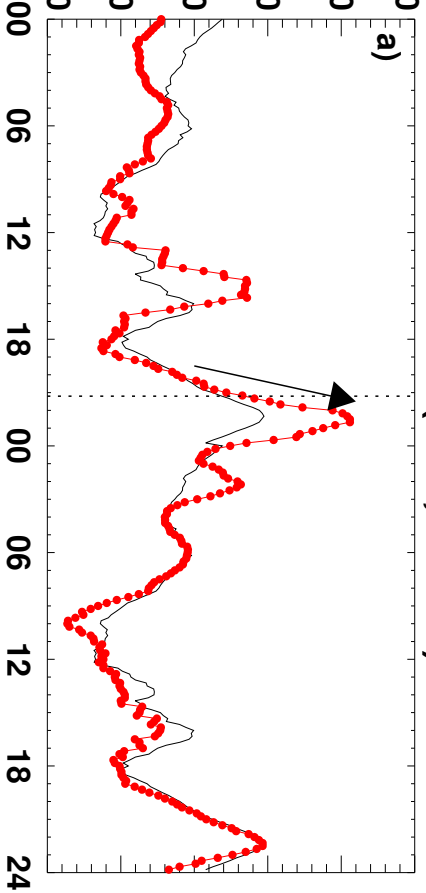
This article is protected by copyright. All rights reserved.

0 10 20 30 40

Figure 4.

Author Manuscript

Sao Luis (2.6S, 315.8E)



Fortaleza (3.9S, 321.6E)

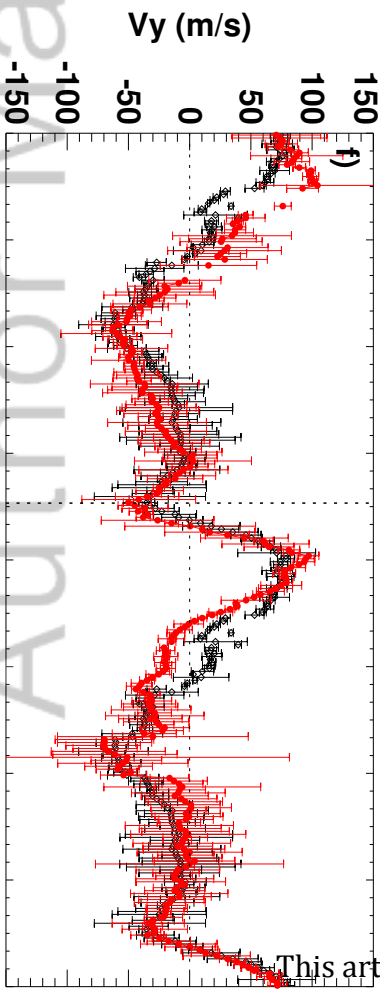
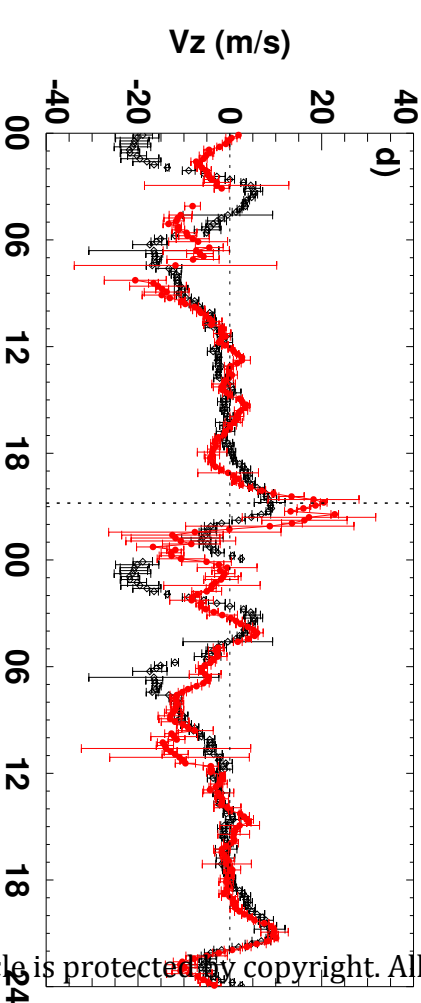
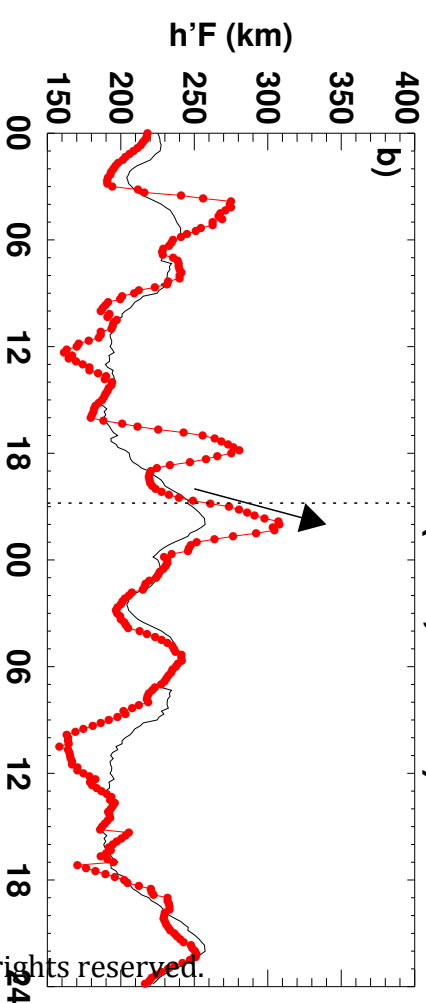
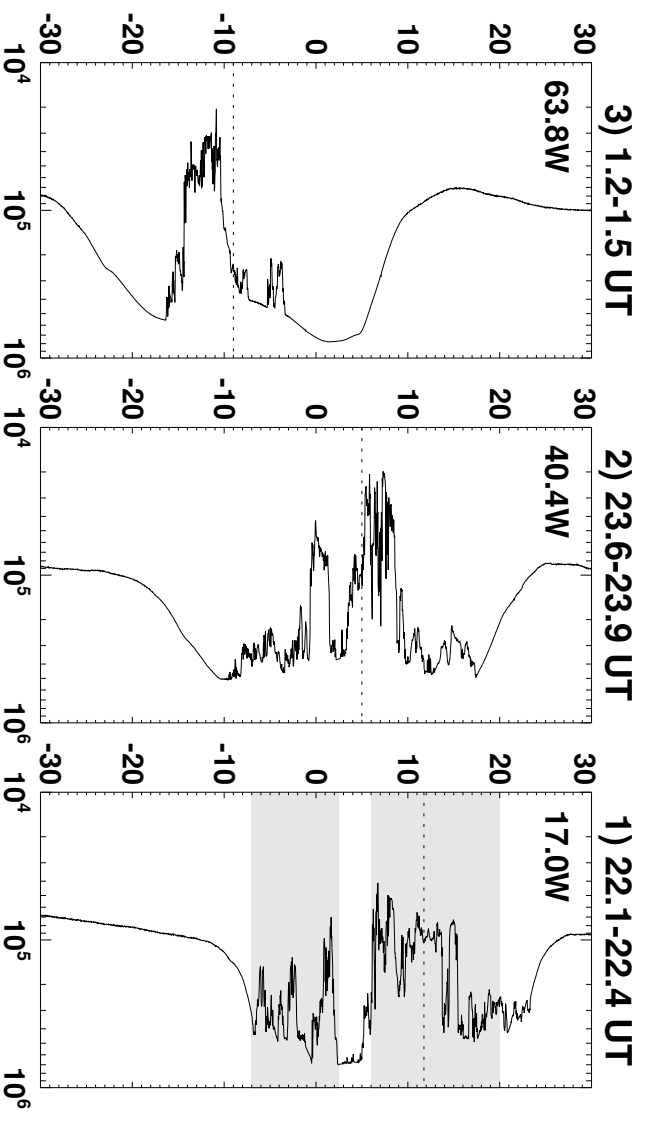
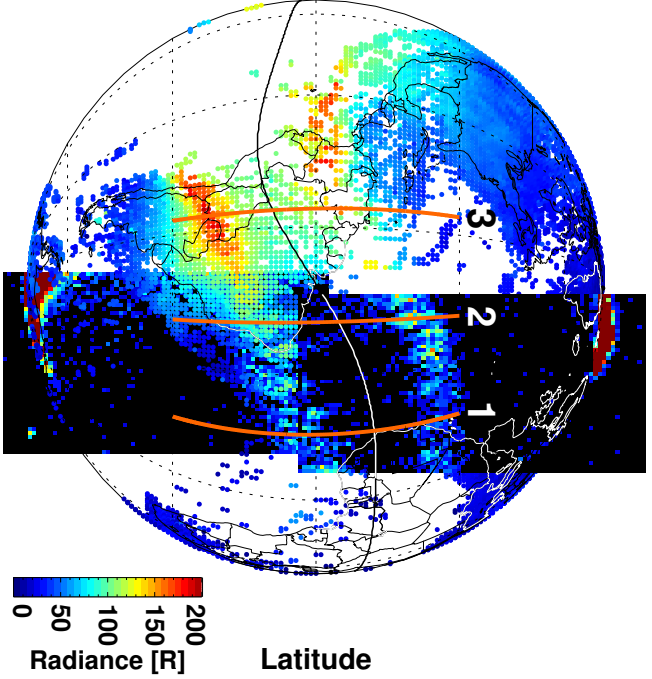
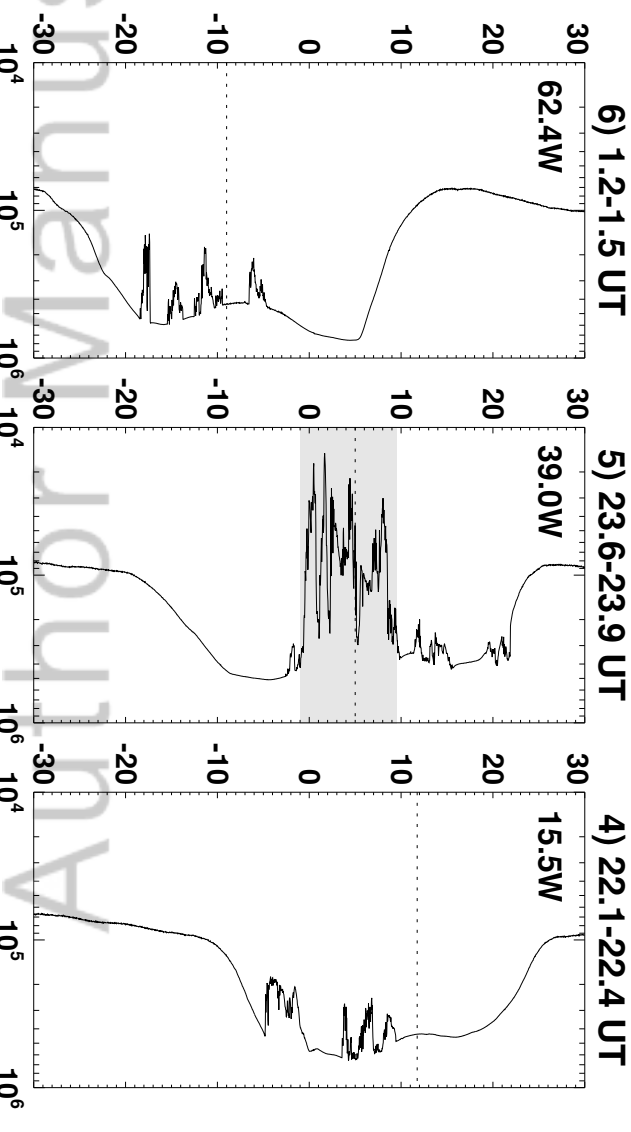
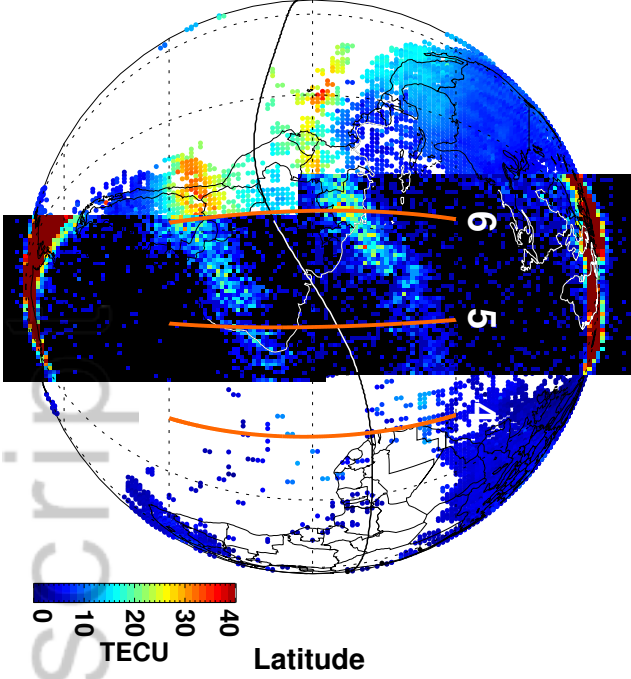


Figure 5.

Author Manuscript



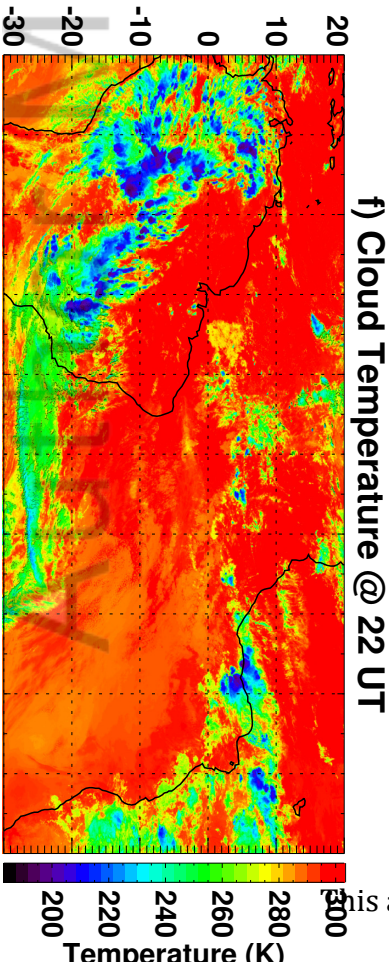
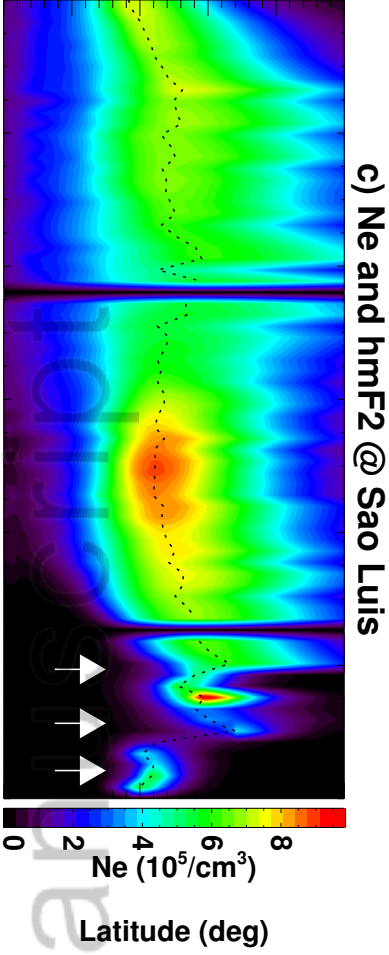
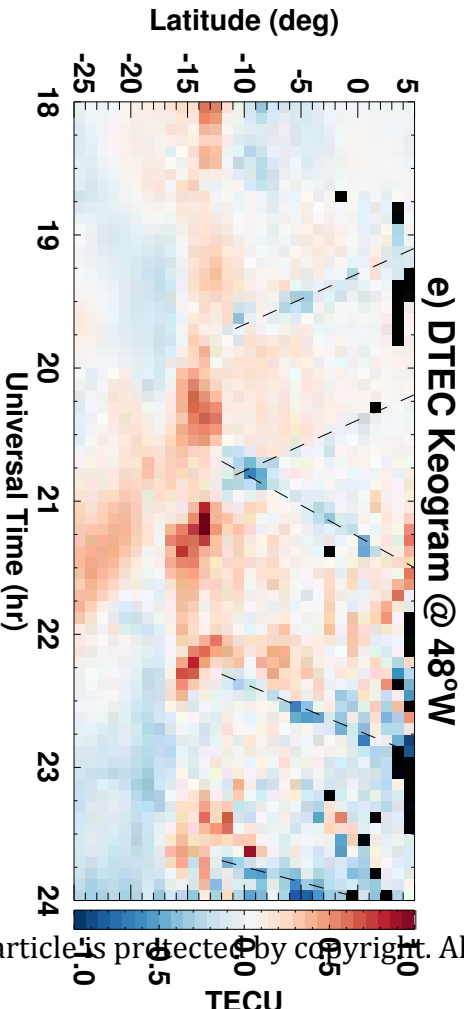
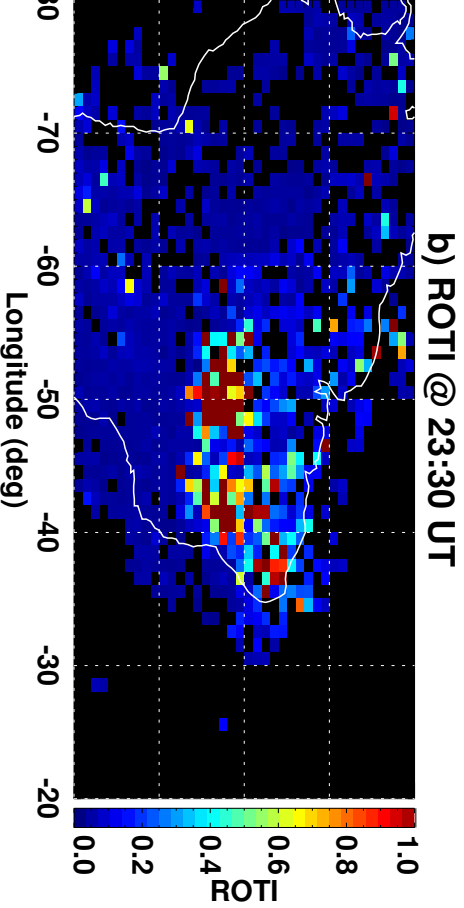
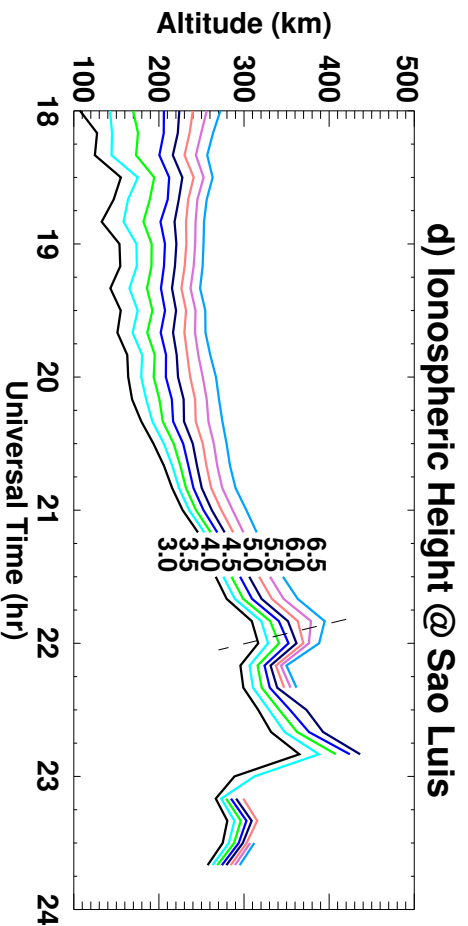
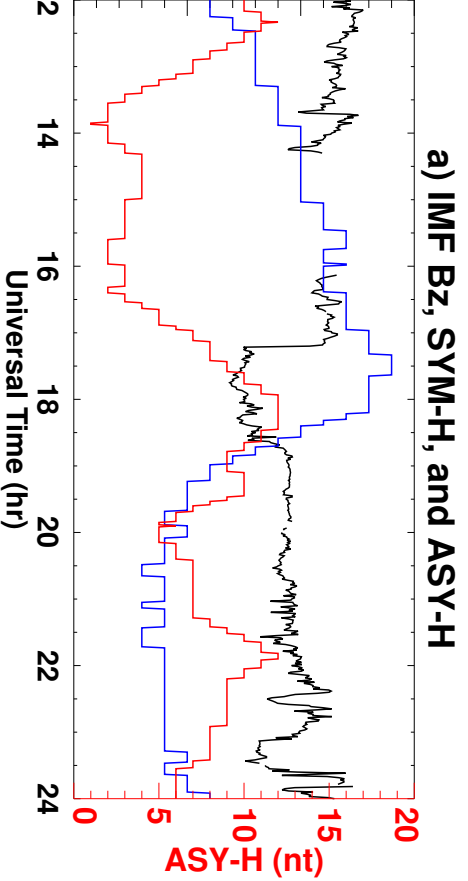
c) GOLD/UV & TEC @ 23:40 UT



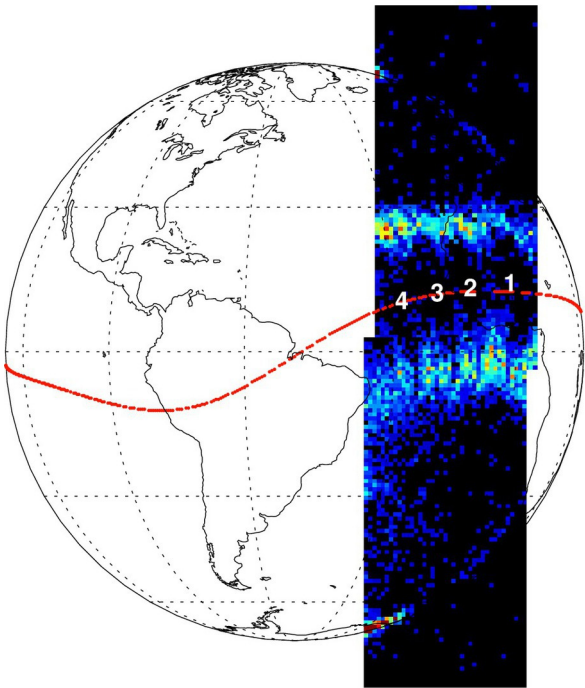
d) Swarm C in-situ Ne ($\#/cm^3$, Altitude = ~ 450 km, MLT = 21.3)

Figure 6.

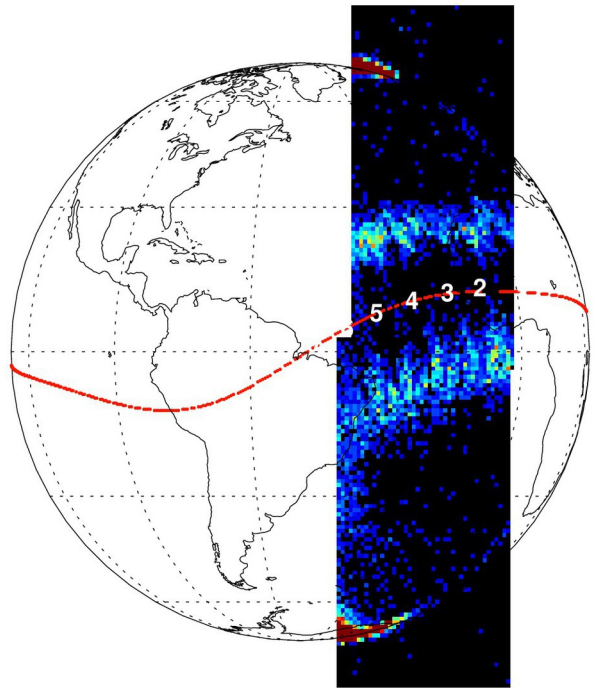
Author Manuscript



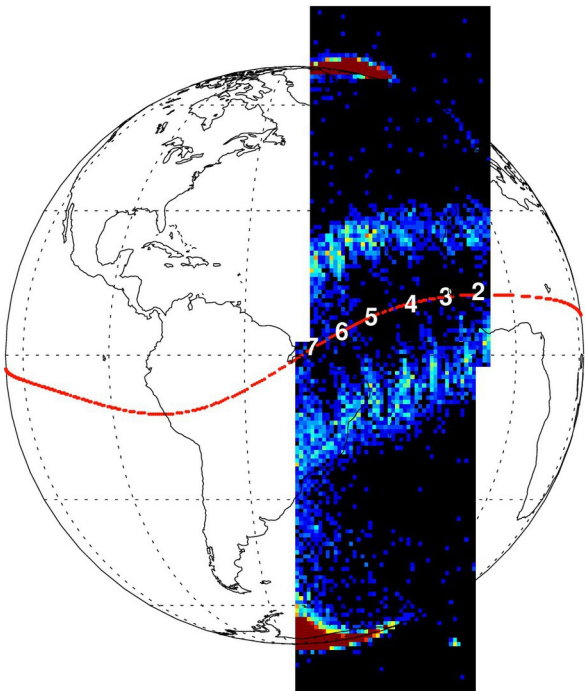
a) 2018-Oct-24 21:10 & 21:25 UT



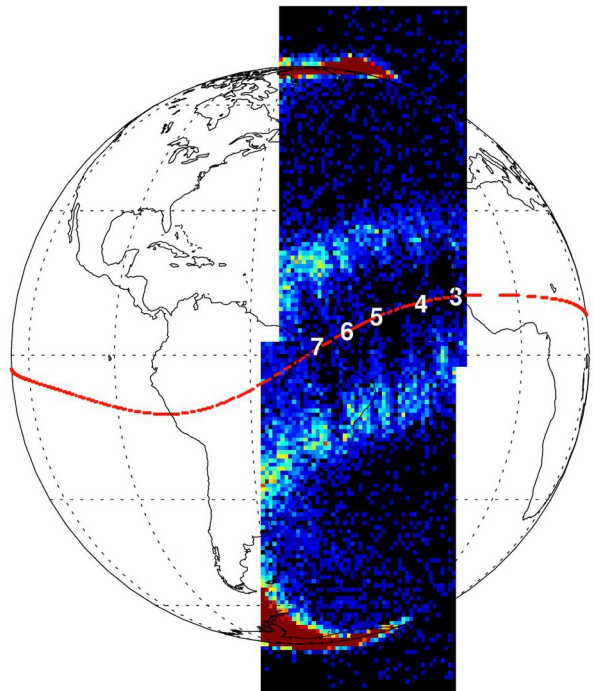
b) 2018-Oct-24 21:40 & 21:55 UT



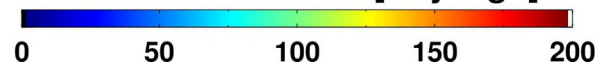
c) 2018-Oct-24 22:10 & 22:25 UT



d) 2018-Oct-24 22:40 & 22:55 UT

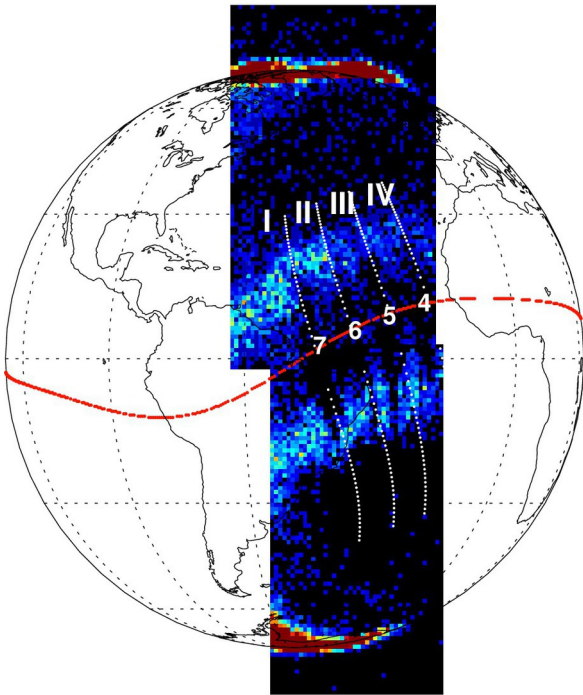


135.6 nm Radiance [Rayleigh]

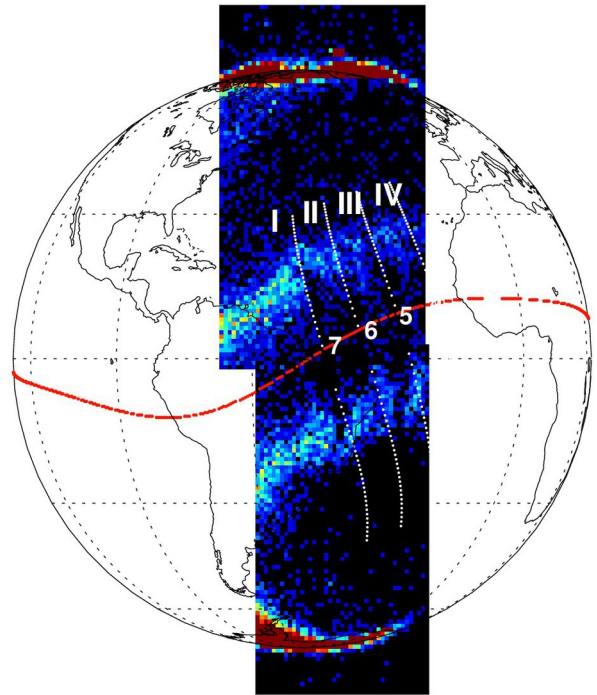


2019ja027569-f01-z-eps

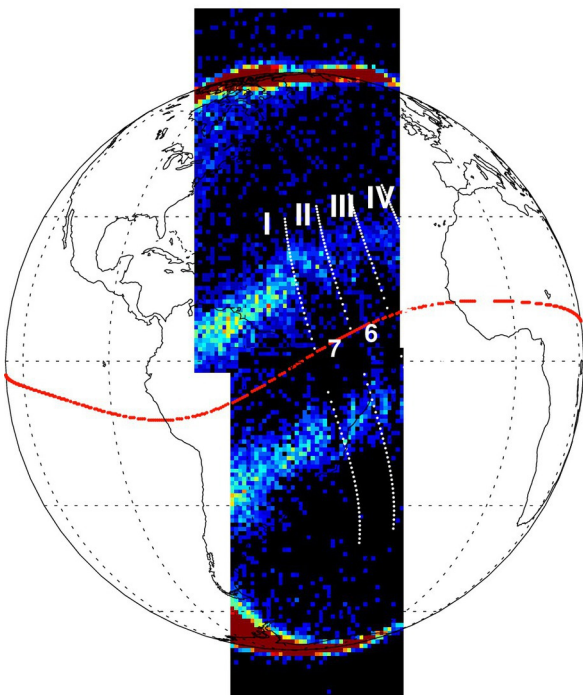
a) 2018-Oct-24 23:10 UT



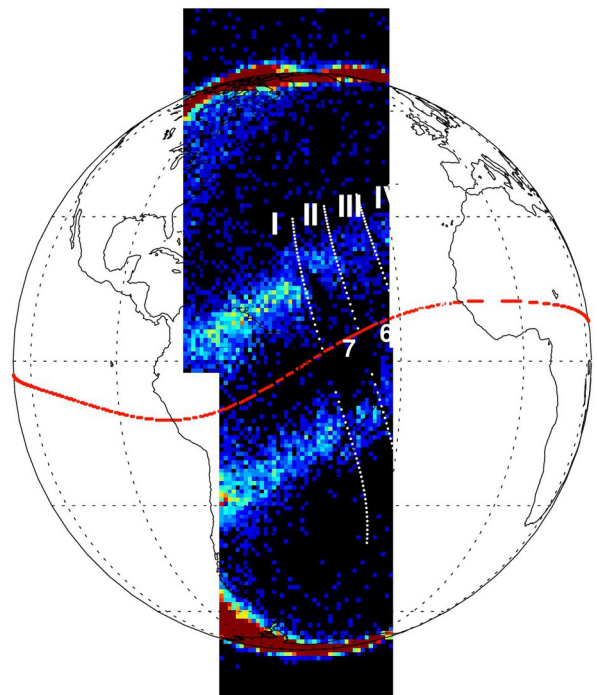
b) 2018-Oct-24 23:25 UT



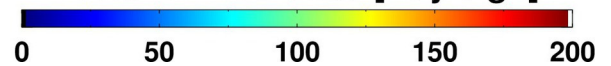
c) 2018-Oct-24 23:40 UT



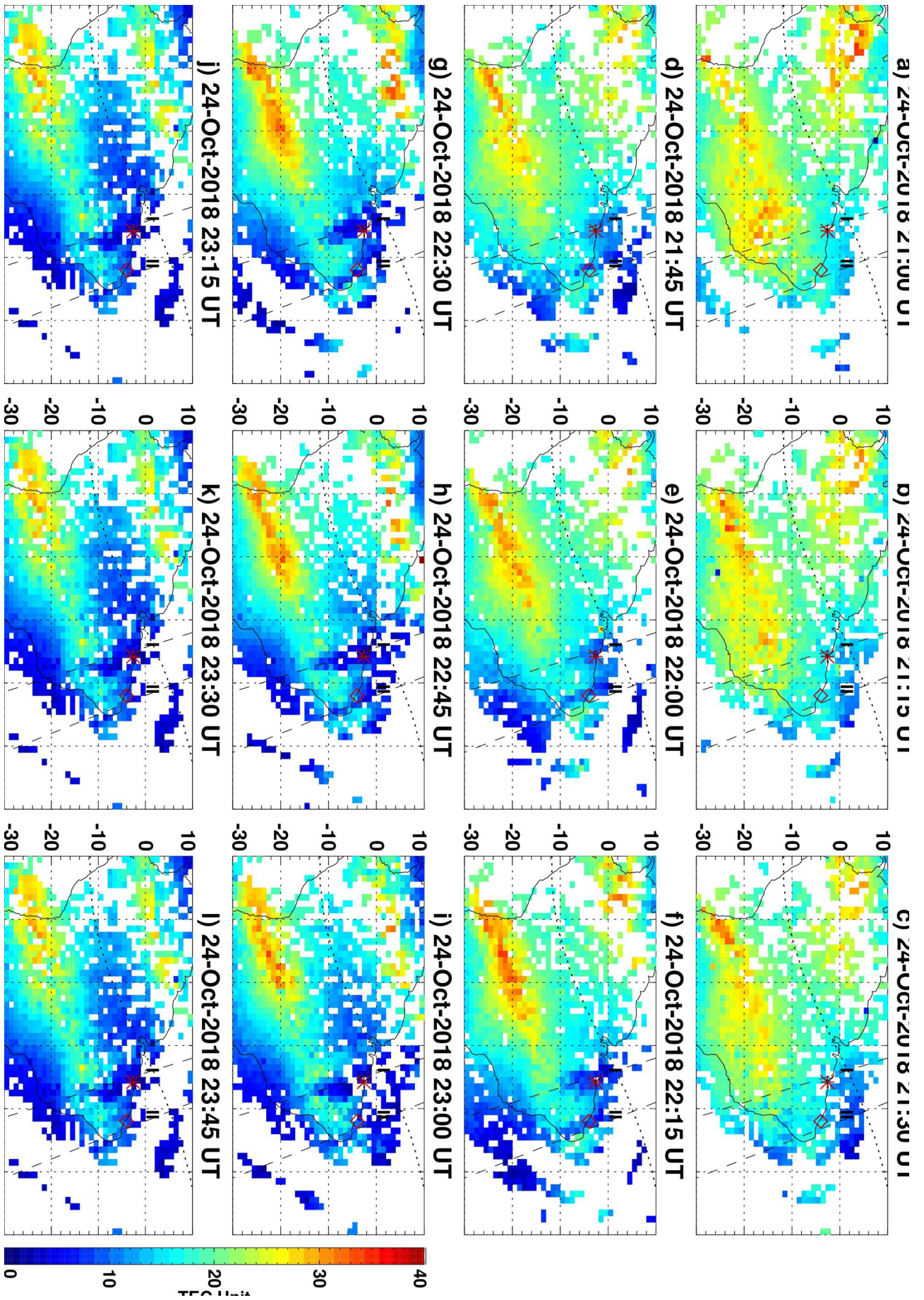
d) 2018-Oct-24 23:55 UT



135.6 nm Radiance [Rayleigh]

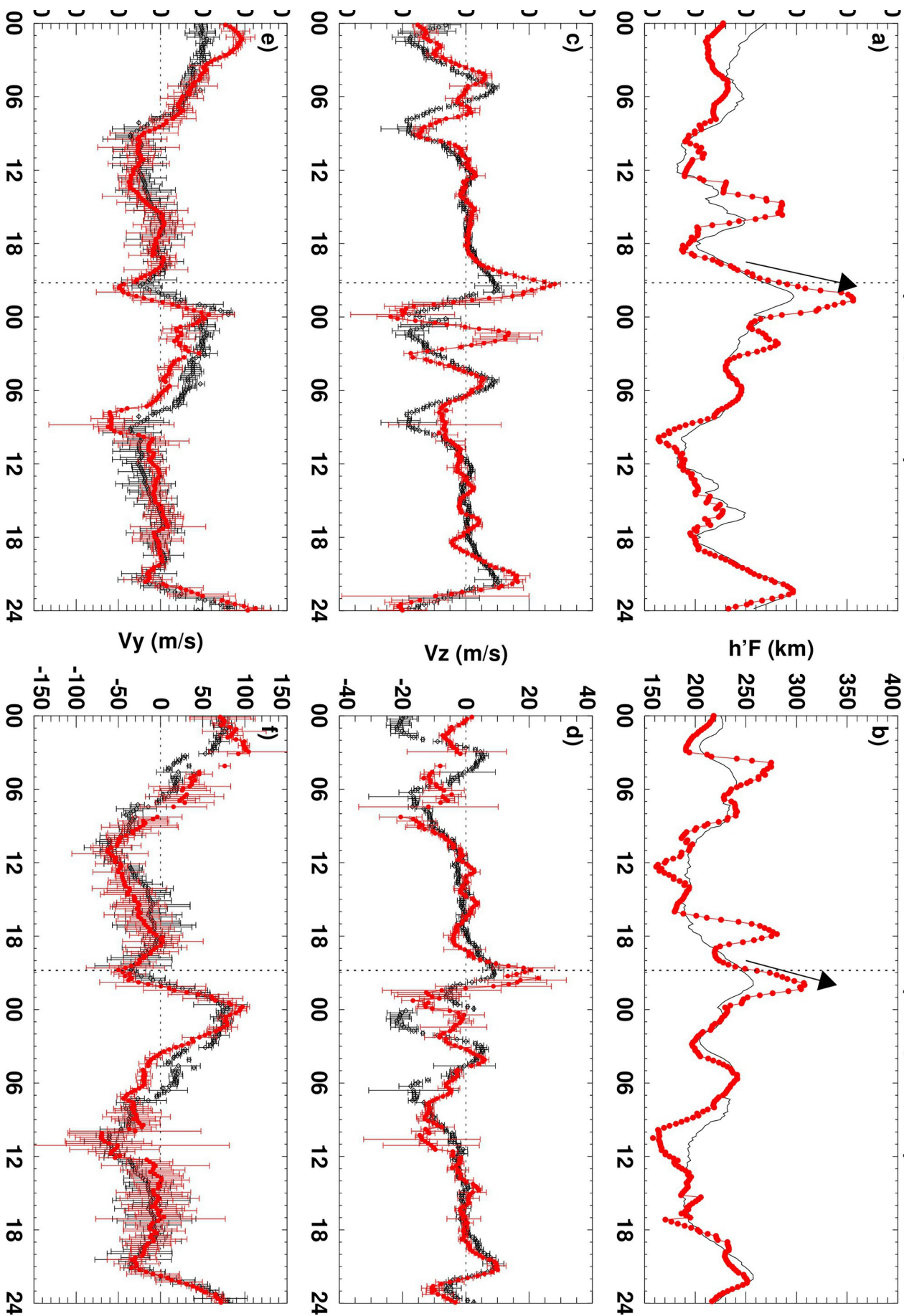


2019ja027569-f02-z-eps

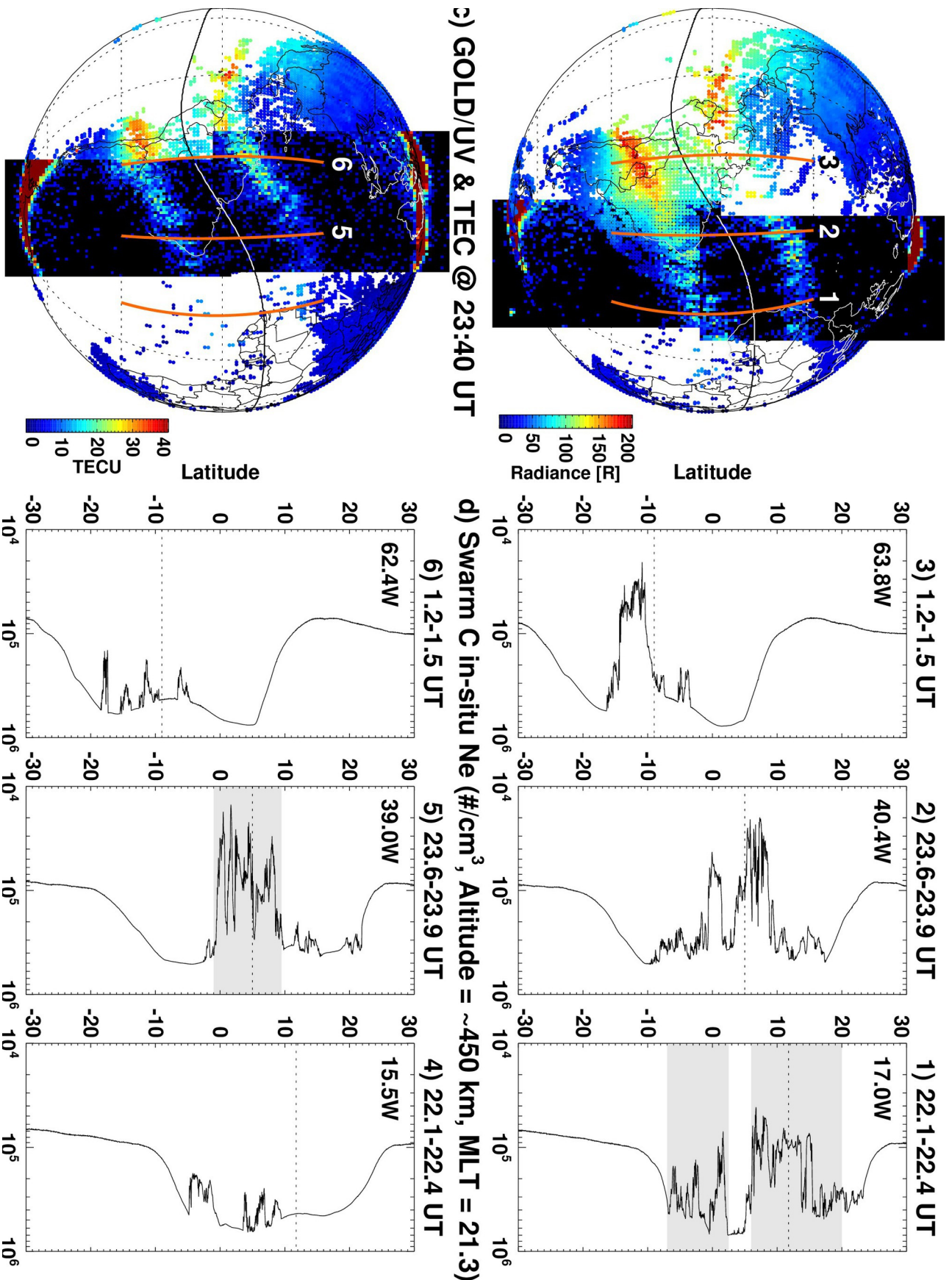


Sao Luis (2.65, 315.8E)

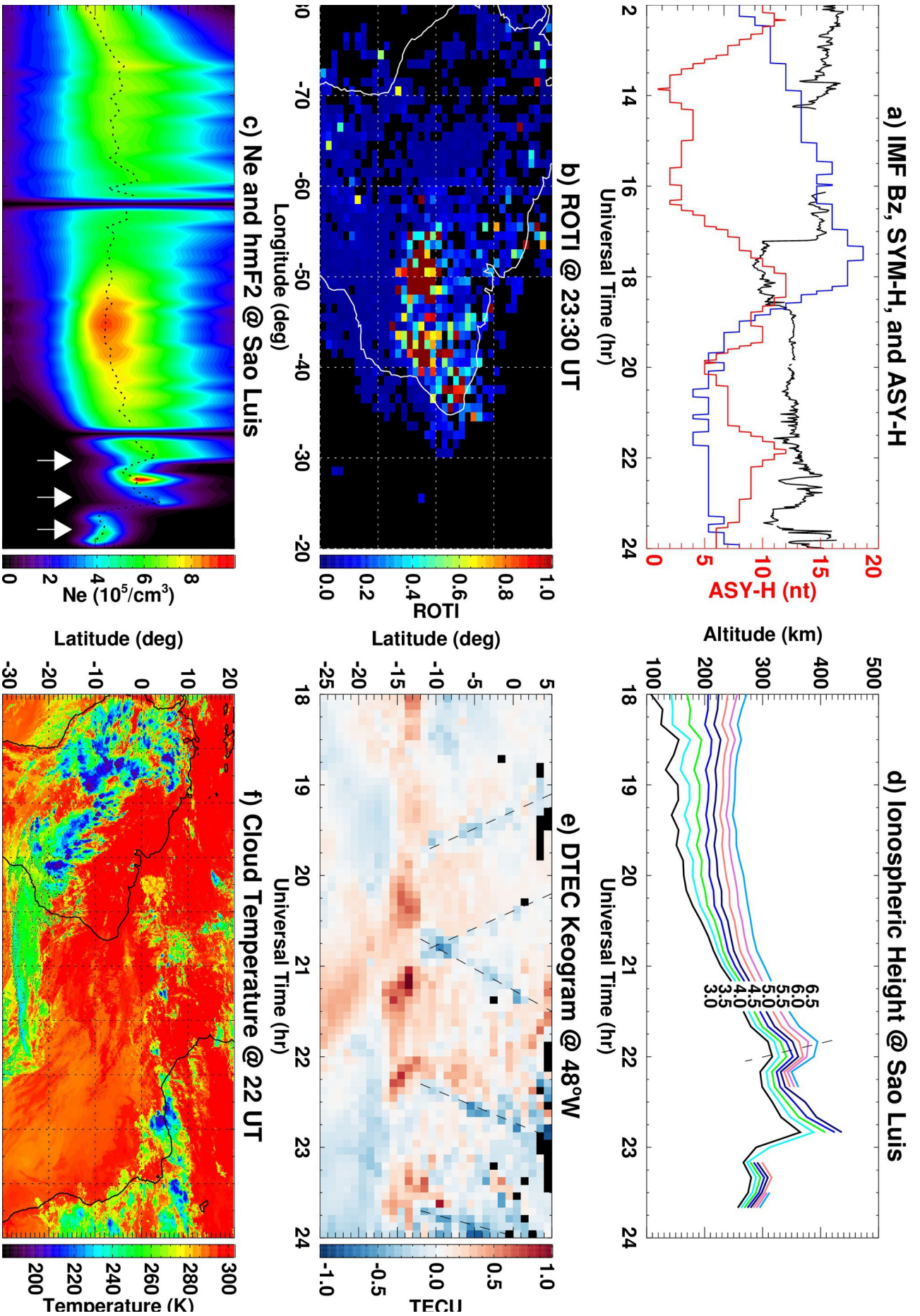
Fortaleza (3.95, 321.6E)



2019ja027569-f04-z-.eps



2019ja027569-f05-z-.eps



2019ja027569-f06-z-.eps